Conservation of Heat in the Coupled Arctic Prediction System (CAPS v1.1): Comprehensive model evaluation based on the MOSAiC observations

Chao-Yuan Yang[1], Fengguan Gu[1], Jiping Liu[1], Annette Rinke[2], Hu Yang[1], Xiaoxu Shi[1]

[1]Southern Marine Science and Engineering Guangdong Laboratory (Zhuhai) and School of Atmospheric Sciences, Sun Yat-sen University, Zhuhai, Guangdong, China

[2]Alfred Wegener Institute, Helmholtz Centre for Polar and Marine Research, Potsdam, Germany

Corresponding authors:

Fengguan Gu (gufg3@mail.sysu.edu.cn) and Jiping Liu (liujp63@mail.sysu.edu.cn)

Abstract

Atmosphere–sea ice–ocean interactions are vital for understanding past and future changes in the Arctic climate system. Consistent heat-flux exchange across model-component interfaces is essential for investigating these interactions with coupled models on longer timescales. Here, we present the improved version of the Coupled Arctic Prediction System (CAPS), in which heat-flux exchange between the atmosphere (WRF) and ocean–sea ice (ROMS–CICE) components is made consistent across coupling interfaces. A set of pan-Arctic simulations covering the period of Multidisciplinary drifting Observatory for the Study of Arctic Climate (MOSAiC) were conducted with the revised CAPS. The revised coupling substantially reduces interfacial heat-flux residuals and improves the simulation of Arctic sea-ice conditions relative to the original coupling, which produces enhanced winter ice growth and reduced summer ice retreat during the 14-month simulation. CAPS was further evaluated against comprehensive MOSAiC observations of the atmosphere, ocean, snow, and sea ice. The model reproduces the broad evolution of Arctic conditions along the MOSAiC drift, although biases remain, partly associated with errors in simulated synoptic systems and unresolved polar physical processes. The constrained-atmosphere experiment with spectral nudging shows improved agreement with observations in several quantitative metric, particularly for atmospheric profiles and ocean temperature. However, sensitivity experiments indicate that these improvements depend on the vertical extent and strength of nudging and should not be attributed to the revised coupling or model physics alone. Remaining biases in atmospheric humidity, surface turbulent heat fluxes, snow accumulation, and ocean salinity

highlight priorities for further development of atmospheric boundary-layer, cloud radiation, snow/sea ice, and coupled surface processes in CAPS and other Arctic prediction systems.

1. Introduction

The Arctic climate system has been undergoing drastic changes and has transitioned toward a new state. Arctic sea-ice extent (SIE) has been decreasing with rates of -0.52 (annual-mean), -0.37 (March-mean), and -0.78 (September-mean) million km^2 per decade over the period of 1979-2024 (Meier et al., 2024; Roach and Meier, 2025). The decline of summer SIE also exhibits a mixture of different rates with the faster period of 1992-2006 (-0.99 million km^2 per decade) and the slowed-down period of 2007-2021 (-0.07 million km^2 per decade) (Polyakov et al., 2023). Arctic sea-ice thickness (SIT) has also decreased from a peak of 3.6 m (winter) / 2.7 m (fall) in 1980 to 2 m / 1.3 m in recent years, which is largely a result of multi-year ice coverage replaced by first-year ice coverage (Kacimi and Kwok, 2024). Corresponding to the slowed-down of summer SIE decline, satellite records also show near-negligible thickness trends since 2007.

In addition to dramatic changes in sea-ice properties, near-surface air temperature in the Arctic regions is warming three to four times faster than the global average, a phenomenon known as Arctic amplification, which is closely linked to sea-ice changes (Holland and Bitz, 2003, Rantanen et al., 2022; Screen and Simmonds, 2010). Over the past two decades, the Arctic Ocean, specifically in the Beaufort Gyre region, has shown a notable accumulation of freshwater (e.g., Timmermans and Toole, 2023), which is associated with sea-ice decline and wind strengthening (e.g., Giles et al., 2012; Wang et al., 2025). Besides the increases of freshwater content in the Beaufort Gyre, sea-ice decline also plays a role in recent warming of Atlantic Water layer in the Arctic Eurasian basin, a phenomenon known as Arctic atlantification

(Polyakov et al., 2017; Wang et al., 2024). Changes in the Arctic described above may also have wider impacts outside of the Arctic, such as extreme weather events in mid-latitude (e.g., Cohen et al., 2014; 2020), and the releasing of freshwater from the Beaufort Gyre into the North Atlantic influencing the Atlantic Meridional Overturning Circulation (e.g., Zhang et al., 2021). Accurately simulating Arctic sea-ice and climate is crucial due to profound impacts of the Arctic on regional weather and climate patterns, and ocean dynamics.

Previously, we developed a Coupled Arctic Prediction System (CAPS; Yang et al., 2020; 2022) designated for seasonal Arctic sea-ice and climate prediction. Experimental seasonal Arctic sea-ice predictions conducted in Yang et al. (2020; 2022) have demonstrated that CAPS has the potential to provide skillful Arctic sea-ice predictions at seasonal timescales. Despite the promising performance of CAPS in seasonal sea-ice predictions, CAPS nevertheless does not fully consider the energy closure between the atmosphere and ocean components through surface heat fluxes, which prevents the applications of CAPS for longer timescales, such as the COordinated Regional Climate Downscaling EXperiment (CORDEX; Gutowski et al., 2016). Discontinuities in surface fluxes and/or numerical errors, which disrupt the conservation of heat or moisture across components in the earth system (e.g., Liepert and Previdi 2012; Lucarini and Ragone 2011; Rahmstorf, 1995), are key factors for the issue of climate drift in climate models (e.g., Irving et al., 2021; Sen Gupta et al., 2013). Atmosphere–sea ice–ocean interactions through variations in surface fluxes are also crucial for climate variability in Arctic sea-ice cover (e.g., Deng and Dai, 2019), and remote impacts of Arctic sea-ice on El Niño–Southern Oscillation (e.g., Deng and Dai, 2024; Liu et al., 2022).

Conservation in coupled models can refer to several related but distinct issues. In many coupled modeling systems, coupler-level conservation is primarily associated with conservative remapping, temporal averaging, and area-weighted merging of fields exchanged between model components on different grids (Craig et al., 2017). In some systems, selected interface fluxes are also calculated centrally in the coupler or mediator (e.g., Danabasoglu et al., 2020; Karsten et al., 2024). These approaches are essential for reducing artificial sources or sinks associated with interpolation, coupling frequency, and component-grid mismatch. However, they do not by themselves guarantee that different model components use physically consistent surface fluxes if those fluxes are re-calculated independently within multiple model components. The issue addressed in CAPS is closer to latter problem. Because all CAPS components use the same horizontal grid, the revised coupling approach presented in this study targets the flux inconsistency caused by parallel calculations of related surface heat fluxes in CAPS (see Section 2 for details). Similar issues have recently been highlighted in regional polar coupled modeling. For example, Malyarenko et al. (2023) developed P-SKRIPS for the Ross Sea region by importing heat and mass fluxes calculated by the atmospheric component directly into the ocean-sea ice component under the same horizontal grid, thereby avoiding duplicated flux calculations and double scaling over mixed sea ice grid cells. Their study demonstrated that such inconsistencies can produce substantial flux mismatches in polar coupled simulations.

In addition to the importance of long-term energy conservation, a unified treatment of surface heat fluxes is also essential for the further development of CAPS as a process-oriented

coupled Arctic framework. The duplicated calculation of surface heat flux makes the implementation of additional surface processes difficult, because new parameterizations must be introduced independently in the atmosphere and ocean–sea ice components while still maintaining consistency across the coupled interface. This issue becomes particularly relevant for future and ongoing CAPS developments involving wave-ice interactions, in which wave-induced surface heat flux changes can directly affect atmosphere–sea ice–ocean exchanges. Therefore, improving the conservation and consistency of surface heat fluxes is a necessary step toward both reducing artificial coupled model-drift and enabling more physically consistent extensions of CAPS.

The Multidisciplinary drifting Observatory for the Study of Arctic Climate (MOSAiC; Nicolaus et al., 2022; Rabe et al., 2022; Shupe et al., 2022) was conducted from September 2019 to October 2020 aboard the Research Vessel *Polarstern* (Knust, 2017). MOSAiC was the largest-scale Arctic research expedition to date and provided comprehensive observations of atmosphere, sea ice, snow, and oceanic physical, chemical, and biological properties in the Arctic climate system. The MOSAiC campaign took place 22 years after the previous year-long Surface Heat Budget of the Arctic Ocean campaign (SHEBA; Uttal et al., 2002). Unlike SHEBA, which was conducted over multiyear sea ice, MOSAiC was conducted over thinner and more dynamic first-year sea ice, with the aim of improving our understanding and model representation of the coupled Arctic climate system under global climate change.

In this study, we aim to resolve a legacy surface heat-flux inconsistency in CAPS to minimize the inconsistency of heat-flux exchange between the atmosphere and ocean–sea ice

components, and to evaluate the revised CAPS comprehensively. Compared with previous regional polar flux-conservation studies, the present work focuses on a pan-Arctic atmosphere–ocean–sea-ice coupling framework, applies the revised coupling over a year-long MOSAiC drift, and evaluated the atmosphere, ocean, and sea-ice components against satellite-derived sea ice products and MOSAiC observations. This paper is structured as follows. Section 2 provides an overview of CAPS focusing on the coupling approach, describes the design of numerical experiments and the model configurations for the model evaluation, and the data measured throughout the MOSAiC campaign. Section 3 presents the evaluation of improved CAPS based on satellite-observed sea-ice conditions and the MOSAiC observations. Concluding remarks and discussions are provided in section 4.

2. Methods and Data

2.1 Coupled Arctic Prediction System

CAPS consists of the Weather Research and Forecasting Model (WRF version 4.1.2), the Regional Ocean Modeling System (ROMS version 3.8), and the Community Ice CodE (CICE version 6.0.0). The data exchange between WRF and ROMS is achieved by the Model Coupling Toolkit (MCT; Larson et al., 2005). Instead of exchanging data through MCT, CICE is embedded within ROMS as subroutines. The integrated ROMS and CICE use the same model time step to better reflect that temperature and salinity of the surface layer will be instantaneously adjusted under supercooled conditions in ROMS, and the freezing/melting potential is calculated accordingly for CICE to form/melt sea ice (adapted from Smith et al., 2010). The required forcing variables of CICE held by ROMS and the CICE-derived variables

144 to ROMS are exchanged through the ROMS–CICE internal coupler every oceanic/sea-ice time
145 step. All model components of CAPS use the same horizontal model grid so that the data
146 exchange between model components does not involve horizontal interpolation.

147 **2.1.1 Original coupling approach**

148 Turbulent heat fluxes of ice-covered ocean cells in WRF and ROMS are based on the
149 mosaic method:

162 $$F = (1 - A_{ice}) \times F_{ao} + A_{ice} \times F_{ai/io}, \qquad (1)$$

150 where F is the summed turbulent heat flux for driving the boundary layer physics in WRF or
151 as the vertical boundary conditions in ROMS, F_{ao} is turbulent heat flux at the atmosphere–
152 ocean interface, $F_{ai/io}$ is turbulent heat flux at the atmosphere–ice or the ice–ocean interface,
153 and A_{ice} is sea-ice concentration. Figure 1 shows the schematic of turbulent heat flux
154 calculation in CAPS. On the ROMS side, F_{io} is provided by CICE based on a Rossby similarity
155 law (Maykut and McPhee, 1995) and F_{ao} is based on the Coupled Ocean–Atmosphere
156 Response Experiment (COARE) 3.0 bulk formula (Fairall et al., 2003). On the WRF side, F_{ai}
157 is computed by the Noah land surface physics (Chen and Dudhia, 2001) and F_{ao} is calculated
158 by the COARE 3.0 algorithm. However, CICE calculates its own F_{ai} with a stability-based
159 boundary parameterization (Jordan et al., 1999). Also, WRF and ROMS do not share the same
160 modifications for implementing the COARE 3.0 algorithm. In other words, the heat flux
161 inconsistency exists at the WRF–ROMS/CICE interface in the original CAPS (Fig. 1a).

163 **2.1.2 Revised coupling approach**

164 To address the inconsistency in turbulent heat flux calculation within CAPS, only one

model component is designated to calculate turbulent heat fluxes for all interfaces (Fig. 1b), i.e., turbulent heat flux calculations at the atmosphere–ice and atmosphere–ocean interfaces are revised. Specifically, WRF determines turbulent heat fluxes at the atmosphere–ocean interface based on the COARE 3.0 parameterization for ROMS to receive. Turbulent heat fluxes at the atmosphere–ice interface are calculated in CICE based on wind fields, potential temperature, and specific humidity of the lowest atmospheric level, and the corresponding height from WRF (see Table 1), and CICE-derived heat fluxes are transferred to WRF.

In addition to turbulent heat fluxes, the related variables (i.e., surface temperature, albedo, and emissivity) involved in the radiation physics in WRF also use the same mosaic approach as in Eq. (1) for ice-covered cells. Both WRF and ROMS use 0.06 as the ocean surface albedo. As for the ice surface albedo, the delta-Eddington scheme in CICE determines the absorption of downward shortwave radiation at the ice surface (Briegleb and Light, 2007), which influences the ice surface albedo diagnostic. However, the original ice surface albedo diagnostic based on the delta-Eddington scheme occasionally returns out of bound values (i.e., larger than one), and zero ice surface albedo in case of zero downward shortwave radiation (e.g., polar night regions). The following approach is applied in CICE to provide full coverage of ice surface albedo, α_{ice}, to WRF:

$$\alpha_{ice} = \begin{cases} (F_{swdn} - F_{swabs})/F_{swdn} & if\ F_{swdn} > 0 \\ \alpha_{ccsm} & if\ F_{swdn} = 0 \end{cases}, \qquad (2)$$

where F_{swdn} is the downward shortwave radiation from WRF, F_{swabs} is the ice-absorbed shortwave radiation based on the delta-Eddington scheme, and α_{ccsm} is the diagnostic albedo based on the parameterization used in the Community Climate System Model, which is the

function of snow/ice surface temperature, ice thickness, snow thickness, and the spectrum of downward shortwave radiation. The surface emissivity of ocean, 0.984, is used for both WRF and ROMS (Konda et al., 1994), and WRF uses the same value (0.95) as in CICE for the surface emissivity of snow and ice. Warren (2019) reported that ice surface emissivity is 0.92 and snow surface emissivity is 0.98-0.99. Table 1 summarizes the variables that WRF, ROMS, and CICE exchange through the couplers with the improved coupling approach. The variables exchange with the original coupling approach are also summarized in Table S1 in the supplement.

This revised coupling approach is similar in the concept of the flux-conservation approach used in P-SKRIPS (Malyarenko et al., 2023), where fluxes computed by the atmospheric component are imported into the ocean-sea ice component to avoid repeated and inconsistent flux calculations. The implementation in CAPS differs in the flux ownership assigned by interface: WRF is used as the source of atmosphere–ocean turbulent heat fluxes, whereas CICE is used as the source of atmosphere–ice turbulent heat fluxes and transfers these fluxes back to WRF. This design preserves the surface fluxes exchanged between the atmosphere and ocean–sea ice components while retaining the existing WRF–ROMS–CICE coupling structure.

2.1.3 Coupling cycle

The model sequence of each model component in the CAPS based on the revised coupling approach is illustrated in Figure 2. In our implementation of the revised coupling in CAPS, WRF calculates its physical processes for the first atmospheric time step to determine all variables (see Table 1), before the initial data exchange between WRF and ROMS/CICE, which provides non-zero values for precipitation and downward radiative heat fluxes to drive

ROMS/CICE physics until the next data exchange. Originally, the surface layer scheme in WRF updates the values of ice surface (e.g., surface temperature and turbulent heat fluxes). In our implementation, the surface layer scheme still updates the related variables of ice surface to maintain the stability of WRF, but the summed values based on Eq. (1) with the CICE-derived values (turbulent heat fluxes of ice surface, ice surface temperature, and ice surface albedo) are the final output values for the boundary layer scheme and the radiation transfer scheme in WRF.

After receiving values from WRF, ROMS will determine the net heat (net radiative heat fluxes plus turbulent heat fluxes), net salt (evaporation minus precipitation), and momentum fluxes of the ocean surface assuming grid cells are ice-free. Subsequently, CICE receives its required variables (see Table 1) through the ROMS-CICE internal coupler, computes fluxes at the atmosphere–ice and ice–ocean interfaces, and then updates ice state variables to the next sea-ice time step. The computed heat, water, salt, and momentum fluxes at the ice–ocean interface are integrated with the fluxes of ocean surface calculated previously based on Eq. (1) as the final top boundary conditions for ROMS to update its state variables to the next oceanic time step.

As described in Section 2.1, the same horizontal model grid for all model components in CAPS makes WRF demand more computational resources than ROMS/CICE. WRF is also more restrictive in atmospheric time step compared to ROMS. To balance the computational loading between WRF and ROMS/CICE, WRF is configured to integrate more atmospheric time steps before exchanging data with ROMS/CICE in this study, and WRF exchanges data

with ROMS/CICE every oceanic/sea-ice time step (Fig. 2, Tab. 2, and see Sect. 2.2 for the exact setup). Note that all data exchanges are done with instantaneous fields without employing time averaging over a coupling cycle in this study.

2.2 Model configurations and simulation designs

In this study, the model domains of WRF, ROMS, and CICE is the same as the previous pan-Arctic configurations of CAPS (Yang et al., 2022; 2024, and see Fig. S1). The domain includes 320 x- and 440 y- grid points with ~24km horizontal resolution on the polar stereographic projection. Initial and lateral boundary conditions for WRF are generated from the fifth generation of European Centre for Medium-Range Weather Forecasts Reanalysis (ERA5, Hersbach et al., 2023, last access: 30 Nov 2025), with 6-hourly time spacing and a spatial resolution of 0.25 degrees. During the initialization processes of WRF, we specify the initial top of lowest model layer to 10 m, which provides ~5 m for the height of the lowest model layer (z_a, see Table 1), and the remaining model layers (50 layers in total, see Table 2) are determined by the default stretching parameters. Global Ocean Ensemble Physics Reanalysis (GREP) produced by Copernicus Marine Service (https://doi.org/10.48670/moi-00024, last access: 30 Nov 2025) is utilized to create initial and lateral boundary conditions for ROMS and CICE. The ensemble of GREP includes Global Ocean ReanalYses and Simulations (GLORYS2V4), Ocean Reanalysis System 5 (ORAS5), and the CMCC Global Ocean Reanalysis Systems (C-GLORSv7). GREP provides daily mean oceanic and sea-ice states with a spatial resolution of 0.25 degrees, and the ensemble mean is used for ROMS and CICE. Previous studies have shown that GREP can provide reasonable estimates of sea-ice and

oceanic states in the Arctic (Cocetta et al., 2024; Yao et al., 2025).

In this study, three experiments covering the entire period of the MOSAiC expedition, starting from 00 UTC September 1st, 2019, to 00 UTC November 1st, 2020 were conducted, and the three primary experiments serve different purposes. Exp_FREE_OLD provides the baseline simulation using the original coupling approach. Exp_FREE uses the revised coupling approach without spectral nudging and is used to evaluate the free-running behavior of the revised CAPS after correcting the heat-flux inconsistency. Exp_NUD uses the revised coupling approach with spectral nudging and is designed as a constrained hindcast experiment in which the large-scale atmospheric state is constrained toward ERA5. The spectral nudging in Exp_NUD is applied to wind, temperature, and humidity, with horizontal wavenumbers 1–3 nudged toward ERA5 data, and only at grid points above the boundary-layer height. The revised coupling approach presented in this study does not guarantee that other physical parameterizations in CAPS are free of biases in polar regions. Previous studies have shown that Arctic weather and climate prediction remains challenging because of limitations in the representation of stable boundary layers, clouds and radiation, atmosphere–ocean–sea-ice exchange, sea-ice/snow processes, and data assimilation under sparse polar observations (e.g., Ortega et al., 2022; Inoue, 2021; Guemas et al., 2016; Vihma, 2014; Hines et al., 2015). Therefore, differences between Exp_FREE_OLD and Exp_FREE primarily reflect the effect of the revised coupling, whereas differences between Exp_FREE and Exp_NUD reflect the sensitivity to the representation of the large-scale atmospheric state. The improved agreement with observations in Exp_NUD should therefore be interpreted as the combined effect of the

revised coupled model and the imposed large-scale atmospheric constraint, rather than as an improvement caused by the revised coupling or model physics alone.

Physical options of each model component are mostly identical to those used in Yang et al. (2024) with several differences for the revised CAPS. For shortwave and longwave radiation, the Rapid Radiative Transfer Model (RRTMG, Iacono et al., 2008) is utilized as the radiation transfer scheme in WRF. The vertical tracer mixing scheme in ROMS is changed to the Large-McWilliams-Doney interior closure scheme, also known as K-profile parameterization (KPP, Large et al., 1994) with several compiling options (controlled by C-preprocessor keywords) activated in ROMS including surface boundary layer mixing (LMD_SKPP), bottom boundary layer mixing (LMD_BKPP, Durski et al., 2004), non-local transport (LMD_NONLOCAL), convective mixing due to shear instability (LMD_CONVEC), double-diffusive mixing (LMD_DDMIX), the effect of shear instability on diffusivity (LMD_RIMIX), and Shapiro filter to boundary layer depth (LMD_SHAPIRO, Shapiro 1970). Further details of physics options and experiment configurations are summarized in Table 2.

2.3 Evaluation data

2.3.1 MOSAiC data

To evaluate the performance of the revised CAPS, the observations from the MOSAiC expedition are utilized, which include radiosondes, the MOSAiC cloud observing suite, meteorological tower, atmospheric surface flux stations (ASFS), conductivity-temperature profiling through depth (CTD) buoys, and snow and ice mass balance array (SIMBA) buoys (Nicolaus et al., 2022; Rabe et al., 2022; Shupe et al., 2022). These observations were

291 distributed within the MOSAiC observational network, including the central observatory (CO),
292 three large sites (L1, L2, and L3) located approximately 15 km from CO, and several medium
293 sites (M1–M8) distributed over a broader area. This distribution of the MOSAiC sites is shown
294 in Fig. 2 of Bliss et al. (2023). For atmospheric observations, radiosondes were launched four
295 times per day, typically at 05, 11, 17, and 23 UTC during MOSAiC. These radiosondes provide
296 vertical profiles from 12 m up to an altitude of about 30 km for temperature, relative humidity,
297 pressure, and winds (Maturilli et al., 2022). The cloud observing suite includes multiple sensors
298 (e.g., cloud radar, depolarization lidar, microwave radiometer, and ceilometer), which provide
299 time-height derivations of cloud microphysical properties (e.g., the cloud type, the condensed
300 water content) (Shupe, 2022). The meteorological tower at Met City (the CO site) measured
301 surface radiative (both downward and upward) heat fluxes with 1-min average intervals.
302 Turbulent heat fluxes were calculated from the tower measurements based on eddy covariance
303 method with 10-min average intervals (Cox et al., 2023). Three ASFS flux measurements,
304 which provide radiative and turbulent fluxes, located at the L1, L2, and L3 sites are also utilized,
305 and these flux measurements will be averaged spatially for the evaluation. For oceanic
306 observations, a set of 8 ice-tethered buoy systems with five CTD units at depths of 10, 20, 50,
307 75, and 100m observing temperature and salinity with 2-min intervals are chosen (Hoppmann
308 et al., 2022). Note that only the CTD-buoy at the M1 site, which provides long records of
309 temperature and salinity, is used for the evaluation. For sea-ice observations, SIT and snow
310 depth measured by SIMBA buoys with 6-hour intervals are used (Lei et al., 2021). SIT can be
311 highly heterogeneous, ranging from a few centimeters to several meters within ~50 km

horizontal distance (e.g., Fig. 2.2 of Haas, 2017). SIT observed by the SIMBA buoys can also be different across each buoy due to the spatial heterogeneity of SIT. Also, the SIMBA buoys were not deployed simultaneously during the MOSAiC expedition, and some buoys only provide relatively short records of SIT and snow depth. SIMBA buoys with relatively long temporal coverage were selected for averaging over their shared period from December 2019 to June 2020. These buoys were located at the CO site (T56, T62, and T66), the L1, L2, and L3 site (T63, T67 and T70), and the M4 site (T58), which was close to CO. The operational periods of SIMBA buoys during MOSAiC are referred to Fig. 2 of Lei et al. (2022). Daily averages from these measurements will be compared with the grid cell nearest to the observations in the modeled daily mean outputs. The track of the MOSAiC expedition started in the northern Laptev Sea, began to move across the central Arctic with the Transpolar Drift, and finally reached the sea-ice edge in Fram Strait (Fig. 1 of Bliss et al., 2023).

2.3.2 Satellite-derived and reanalysis-based sea-ice data

Since the data collected during the MOSAiC expedition can only provide point observations along the drift, satellite-derived and reanalysis-based sea-ice data are also utilized to evaluate the revised CAPS spatially. For sea-ice concentration (SIC), the daily SIC obtained from the National Snow and Ice Data Center (NSIDC) is chosen in this study. The SIC data is measured by Nimbus-7 Scanning Multichannel Microwave Radiometer (SMMR), the Defense Meteorological Satellite Program (DMSP), Special Sensor Microwave/Imagers (SSM/Is), and Special Sensor Microwave Imager/Sounder (SSMIS) passive microwave sensors, and the SIC data is on the NSIDC polar stereographic grid with a spatial resolution of 25 km (NSIDC_0051,

DiGirolamo et al., 2022, last access: 30 Nov 2025). For sea-ice thickness (SIT), the statistically merged SIT based on CryoSat-2 and Soil Moisture and Ocean Salinity satellite data (CS2SMOS, Ricker et al., 2017, last assess: 30 Nov 2025) is utilized. However, satellite-based SIT is not available during the melting season since satellite cannot differentiate the mixture of wet snow/sea ice, melt ponds, and open water (e.g., Huntemann et al., 2014). The daily SIT produced by the Pan-Arctic Ice Ocean Modeling and Assimilation System (PIOMAS, Zhang and Rothrock, 2003) is chosen to fill the data gap in CS2SMOS.

3. Results

3.1 Evaluation

3.1.1. Evaluation of sea-ice concentration and thickness

In this section, we first evaluate the revised CAPS focused on Exp_FREE and Exp_NUD (with Exp_FREE_OLD as reference) against satellite-based sea-ice observations to provide an overview of the performance of revised CAPS in simulating sea-ice conditions over the pan-Arctic domain during the MOSAiC period. Figure 3 shows the evolutions of SIE of the observations, Exp_FREE, Exp_NUD, and Exp_FREE_OLD, as well as the integrated ice-edge error (IIEE, Goessling et al., 2016) of Exp_FREE, Exp_NUD, and Exp_FREE_OLD with respect to the observations. SIE is computed as the summation of areas of all cells with at least 15% SIC, and the observed SIE is calculated from NSIDC-0051 SIC. IIEE is defined as the sum of areas where the simulation and the observation disagree on SIC of the same cell being above or below 15%. The smaller (larger) IIEE indicates that the simulated distribution of sea-ice edges is comparable (different) to the observed distribution. As shown in Fig. 3a, both

354 Exp_FREE and Exp_NUD can reasonably reproduce the seasonal cycle (i.e., the timing of
355 maximum and minimum) of SIE during the MOSAiC period, and both experiments show an
356 underestimation of $1.0\sim1.5 \times 10^6$ km^2 in SIE with respect to the observations around March
357 2020. In general, the evolution of SIE in Exp_FREE (Fig. 3a) shows smaller SIE for 2019/2020
358 winter months (November 2019 to April 2020) and larger SIE for 2020 summer months (June
359 to October 2020) compared to that in Exp_NUD (Fig. 3a). As reference, Exp_FREE_OLD (Fig.
360 3a) simulates larger SIE than Exp_FREE, and the differences in SIE become significantly
361 larger in 2020 summer, indicating the original coupling approach used in the previous version
362 of CAPS (Fig. 1a) may prone to drift to a state with extensive sea-ice coverage as the model
363 integrates for longer period. IIEE of Exp_NUD (Fig. 3b) is generally smaller than that of
364 Exp_FREE (Fig. 3b) for most of the simulation period, suggesting that Exp_NUD shows better
365 performance in simulating the distribution of sea-ice edges than Exp_FREE. Compared with
366 Exp_FREE, Exp_FREE_OLD (Fig. 3b) shows generally smaller IIEE from September 2019 to
367 April 2020 corresponding to better agreement between the simulated SIE in Exp_FREE_OLD
368 and the observed SIE. After July 2020, Exp_FREE_OLD shows generally larger IIEE than
369 Exp_FREE.

370 The monthly averaged March and September SIC fields from the observations in 2020,
371 together with the difference between the simulations and the observations, are shown in Fig. 4.
372 Following the IIEE definition of Goessling et al. (2016), the lined areas in Figs. 4b–d and 4f–
373 h indicate grid cells where the simulated and observed local SIE disagree based on the 15 %
374 SIC threshold. Specifically, underestimated local SIE refers to regions where the observed SIC

375 exceeds 15 % but the simulated SIC does not, whereas overestimated local SIE regions where
376 the simulated SIC exceeds 15 % but the observed SIC does not. Corresponding to the SIE
377 shown in Fig. 3a, the underestimated SIE of Exp_FREE and Exp_NUD in March 2020 mainly
378 arise from underestimated local SIE in the Sea of Okhotsk, the Barents Sea, the Labrador Sea,
379 and Davis Strait (Figs. 4b–c). In contrast to better agreement with the observed SIC shown in
380 Exp_NUD (Fig. 4c, colored areas), Exp_FREE simulates larger SIC in the Bering Sea and
381 smaller ice coverage the Barents Sea in March 2020 (Fig. 4b). Generally, Exp_FREE_OLD
382 shows larger ice coverage (e.g., in the Sea of Okhotsk, and the Barents Sea) than Exp_FREE
383 in March 2020 (Figs. 4b, 4d). In September 2020, the comparable areal coverage of
384 overestimated local SIE along the coasts of Alaska, central Siberia, and eastern Siberia and
385 underestimated local SIE near Fram Strait and the Canadian Archipelago in Exp_FREE
386 contributes to the smaller difference in total SIE relative to the observations (Figs. 3a, 4f). In
387 contrast, underestimated local SIE in the central Arctic Ocean and Canadian Archipelago,
388 partly compensated by overestimated local SIE in the Chukchi Sea, is the main contributor to
389 the underestimated SIE in Exp_NUD (Figs. 3a, 4g). Exp_FREE_OLD shows that most of the
390 Arctic Ocean is covered by ice with at least 15% SIC (Fig. 4h) corresponding to significant
391 overestimation of SIE in summer 2020 shown in Fig. 3a.

392 Figure 5 shows the monthly-averaged March and September SIT of the reference data and
393 the simulations in 2020. The average SIT of all cells with at least 1% SIC for the reference data
394 and the simulations in March and September 2020 are also shown in Figure S2 in the
395 supplement. In March 2020, all experiments can reproduce the general patterns of SIT

compared with CS2SMOS, showing the thickest ice located north of the Canadian Archipelago with decreasing thickness gradient toward Siberia (Figs. 5a–d). However, all experiments show more thicker SIT accumulated in the Western Arctic Ocean, especially along the coastal areas of Alaska and eastern Siberia. Exp_FREE simulates overall thinner SIT (~1.13 m, Fig. S2) in the Arctic Ocean compared with Exp_NUD (~1.16 m, Fig. S2). For regional difference, Exp_NUD show thicker SIT in the north of the Canadian Archipelago and Alaska but thinner SIT along the Siberia coast compared to Exp_FREE (Figs. 5b–c). Corresponding to larger ice coverage of Exp_FREE_OLD in March 2020 (Fig. 4d), Exp_FREE_OLD shows relatively thicker SIT (~1.17 m, Fig. S2) in most of the Arctic Ocean than Exp_FREE (Figs. 5b, 5d). The simulated biases of SIT in September 2020 of both experiments are partly associated with those in March 2020. That is, the thinner SIT along the Siberia coast in Exp_NUD is less persistent, and the thicker SIT along the coastal areas of Alaska and eastern Siberia in Exp_FREE and Exp_NUD in March 2020 is more persistent (Figs. 5b–c, 5f–g). The overestimated and underestimated local SIE in September 2020 (Figs. 4f–g) are also associated with the simulated bias of SIT in March 2020, such as the OLSIE of Exp_FREE and Exp_NUD in the Chukchi Sea, and the underestimated local SIE of Exp_NUD in the central Arctic Ocean. The evolution of SIT from April 2020 to August 2020 shown in Figure S3 in the supplement also illustrates the lasting influence of simulated bias of SIT in March 2020. Generally, Exp_NUD shows better agreement with CS2SMOS and PIOMAS than Exp_FREE in both March and September 2020 (Figs. 5, S2). In Exp_FREE_OLD, most of the Arctic Ocean is still covered by sea ice with the average SIT of 1.25 m in summer 2020 (Figs. 5h, S2), which is significantly thicker

than Exp_FREE (~0.54 m, Fig. S2) and Exp_NUD (~0.59 m, Fig. S2), corresponding to extensive ice coverage in most of the Arctic Ocean shown in Fig. 4h.

3.1.2. Evaluation of improved flux coupling

To diagnose the consistency of heat-flux exchange between the atmosphere and the ocean-sea-ice components with the original and revised coupling approaches, we define the residual of interfacial heat-flux exchange at the atmosphere–ocean–sea-ice coupling cells, which can be expressed as

$$R_{coupling}(x,y,t) = F_{surface}^{WRF}(x,y,t) - F_{surface}^{ROMS/CICE}(x,y,t)\,, \qquad (3)$$

where $F_{surface}^{WRF}$ is the flux component used in the WRF physical processes, and $F_{surface}^{ROMS/CICE}$ is that in the ROMS/CICE processes. Both $F_{surface}^{WRF}$ and $F_{surface}^{ROMS/CICE}$ are the weighted averaged fluxes based on Eq. (1). The flux component is defined as positive downward and includes net surface heat flux (NetHF), with the components of net shortwave radiative flux (NetSW), net longwave radiative flux (NetLW), sensible heat flux (SH), and latent heat flux (LH). Figure 6 shows the domain-mean residual, domain-mean absolute residual, and root-mean-square error (RMSE) of interfacial heat-flux residuals for all flux components in Exp_FREE_OLD, Exp_FREE, and Exp_NUD. Exp_NUD is included in this residual analysis as an additional check that the revised coupling maintains similar interfacial heat-flux residuals under the constrained-atmosphere configuration. Mean residuals of NetHF are 0~15 W/m^2 for most of the simulation period with the original coupling approach (Exp_FREE_OLD), whereas those with the revised coupling approach (Exp_FREE and Exp_NUD) are negligible (less than 0.1 W/m^2, Figs. 6a, S4a). Since all fluxes are defined positive downward, positive (negative)

438 residuals of NetHF represents that the ocean-sea ice component receives less (more) energy
439 than it supposes to receive, which can be also viewed as an artificial cooling (warming) effect
440 in the ocean-sea ice coupled system due to the inconsistency in heat-flux exchange. Mean
441 residuals of NetHF in Exp_FREE_OLD are mainly contributed by turbulent components rather
442 than radiative components (Figs. 6a–e). Mean residuals of SH are mostly positive throughout
443 the simulation, with the magnitude ranging from ~0 to ~12.5 W/m^2 (Fig. 6c). Mean residuals
444 of LH are mostly positive from September 2019 to April 2020 (up to ~11.5 W/m^2) and then
445 negative afterward (up to ~8 W/m^2) (Fig. 6d). For Exp_FREE and Exp_NUD, the mean (Fig.
446 6a–e), mean absolute (Figs. 6f–j), and RMSE residuals (Figs. 6k–o) remain much smaller than
447 those in Exp_FREE_OLD, confirming that the revised coupling substantially reduces both the
448 systematic and local/intermittent interfacial heat-flux residuals. The remaining residuals are
449 generally small and mainly reflect numerical and diagnostic differences rather than the large
450 systematic inconsistency seen in Exp_FREE_OLD. The contrast between Exp_FREE_OLD
451 and Exp_FREE demonstrates the effect of the revised coupling itself, because both experiments
452 are free-running and differ primarily in the coupling approach. The similarly small residuals in
453 Exp_NUD indicate that the revised coupling remains consistent when spectral nudging is
454 applied.

455 To place the interfacial residuals shown in Fig. 6 into a coupled-system energy-cycle
456 context, we further diagnose the daily integrated energy exchange through the lower boundary
457 of the atmosphere, the atmosphere–ice and ice–ocean interfaces of sea ice, and the upper
458 boundary of the ocean for Exp_FREE_OLD and Exp_FREE (Fig. 7). Positive values represent

459 energy gain by the component or interface indicated in each panel. Because the purpose of
460 Figure 7 is to isolate the effect of the coupling revision on the component-level energy
461 pathways, we compare Exp_FREE_OLD and Exp_FREE only; Exp_NUD is not included in
462 this diagnostic because it additionally differs by the use of spectral nudging. Both experiments
463 reproduce a pronounced seasonal surface energy cycle. The atmosphere gains energy from the
464 surface during the cold season and loses energy during the melt season, while the ocean shows
465 the opposite seasonal behavior, with heat loss in autumn–winter and heat uptake in late spring–
466 summer (Figs. 7b–c). These domain-integrated atmospheric and oceanic exchanges are mainly
467 controlled by open-ocean grid cells, as indicated by the close correspondence between the total
468 atmospheric/oceanic energy terms and their open-ocean contributions (Figs. 7h–i), while the
469 ice-covered and land-cell contributions are smaller in magnitude (Figs. 7e, f, j).

470 The sea-ice net exchange is roughly one order of magnitude smaller than the atmospheric
471 and oceanic exchanges but is more directly linked to the simulated sea-ice thermodynamic
472 response. Sea ice loses energy from autumn to early spring and gains energy during the melt
473 season, with a peak in early summer (Fig. 7a). This seasonal transition is mainly controlled by
474 the atmosphere–ice interface: sea ice loses energy to the atmosphere during the cold season and
475 gains energy from the atmosphere during late spring and summer (Fig. 7d). Compared with
476 Exp_FREE, Exp_FREE_OLD generally shows stronger negative atmosphere–ice exchange
477 during winter and weaker positive atmosphere–ice exchange during summer, indicating
478 enhanced cold-season energy loss from sea ice and reduced melt-season atmospheric energy
479 input to sea ice in the original coupling approach. Although differences in the domain-

integrated atmospheric and oceanic exchanges are relatively small because they are dominated by open-ocean cells, the differences over ice-covered cells are more evident and directly affect the sea-ice energy pathway. This helps explain why the original coupling approach leads to a cumulative overestimation of sea-ice thickness and coverage during the 14-month simulation, characterized by enhanced winter ice growth and reduced summer ice retreat (Figs. 3–5). This diagnostic represents the surface/interface energy exchange among model components rather than a fully closed three-dimensional prognostic heat budget for each component, because atmospheric and ocean heat storage, lateral boundary transports, and internal source-sink terms are not explicitly included.

To further illustrate how the inconsistency in surface heat fluxes degrades the performance of CAPS with the original coupling approach in Exp_FREE_OLD, the evolutions of sea-ice volume (SIV) budget components (with their terminology according to Appendix E of Notz et al., 2016) for Exp_FREE and Exp_FREE_OLD are compared (Fig. 8). Overall, the total SIV tendencies in Exp_FREE_OLD (Fig. 8a) are higher than those in Exp_FREE (Fig. 8a) for most of the simulation, with largest differences (up to 0.2 cm/day) between both experiments in July 2020 compared to the rest of the simulation. The higher total SIV tendencies in Exp_FREE_OLD indicates that the simulated SIT in Exp_FREE_OLD will become thicker than that in Exp_FREE as the model integrates, which is also shown in the average SIT in March and September 2020 (Fig. S2). The thicker SIT contributes slower retreating of sea-ice coverage during the melting season in Exp_FREE_OLD, corresponding to significantly overestimated SIE shown in Figure 3a. Compared to Exp_FREE, Exp_FREE_OLD shows

501 higher SIV growth rate at the bottom of the ice (basal growth, Fig. 8f) and from supercooled
502 open water (frazil, Fig. 8g) in 2019/2020 winter and spring, and significantly less SIV melting
503 at the atmosphere–ice interface (top melt, Fig. 8b) in summer 2020.

504 Figure 9 shows the heat flux budget components at the atmosphere–ice interface and the
505 ice–ocean interface for both Exp_FREE and Exp_FREE_OLD. Generally, the net heat flux at
506 the atmosphere–ice interface (Fig. 9a) is well correlated to the total SIV tendencies shown in
507 Figure 8a. Larger negative net heat fluxes (i.e., sea ice loses energy to the atmosphere)
508 contribute to larger SIV growth. Accordingly, the larger negative heat flux in Exp_FREE_OLD
509 compared to Exp_FREE drives the larger SIV growth in Exp_FREE_OLD in winter,
510 particularly in January 2020. And, the smaller positive net heat fluxes (i.e., sea ice gains energy
511 from the atmosphere) in Exp_FREE_OLD, compared to Exp_FREE, in July 2020 are
512 responsible for the smaller SIV melting in Exp_FREE_OLD. The decomposition of the net
513 heat fluxes at the ice surface to radiative and turbulent components (Figs. 9c–f) shows that the
514 larger negative net heat fluxes from October 2019 to December 2019 in Exp_FREE_OLD are
515 caused by the combination of latent heat flux and net longwave radiation loss at the surface
516 (which are partially cancelled by oscillated positive sensible heat fluxes). The smaller positive
517 net heat fluxes in Exp_FREE_OLD in July 2020 are mainly dominated by smaller net
518 shortwave radiative fluxes. In contrast to net heat fluxes at the atmosphere–ice interface, net
519 heat fluxes at the ice–ocean interface do not show clear contributions to SIV tendencies in
520 Exp_FREE_OLD (Fig. 8, 9b).

521 **3.1.3. Computational cost estimation**

To document the computational cost of the revised coupling, we conducted 31-day benchmark simulations using the original and revised coupling approaches. Both simulations were integrated from 00 UTC October 1st, 2019 to 00 UTC November 1st, 2019 using identical input/output settings, the same node list, and the same processor layout. Wall time and memory usage were obtained from the SLURM accounting record for the model execution step. The throughput shown in Table 3 is reported as simulated years per wall-clock day (SYPD), calculated as

$$SYPD = \frac{D_{sim}/365}{T_{wall}/24}$$

where D_{sim} is the number of simulated days and T_{wall} is the wall time in hours. The computational cost is also reported as core-hours per simulated year (CHPY),

$$CHPY = T_{wall} \times N_{core} \times \frac{365}{D_{sim}}$$

where N_{core} is the number of allocated cores.

The revised coupling introduces negligible additional wall-clock cost relative to the original coupling. The wall time increases from 3 h 04 min 29 s to 3h 04 min 33 s, corresponding to an overhead of 0.036 %. The throughput remains nearly unchanged, from 0.6629 to 0.6627 SYPD. The estimated computational cost also changes slightly, from 11584.8 to 11588.9 CHPY. These results indicate that the revised heat-flux exchange does not impose a meaningful computational burden under the benchmarked configuration. The present benchmark should be interpreted as a production-configuration overhead estimation rather than a comprehensive scaling test. The current CAPS domain has a moderate horizontal grid size of 320x440, and the production layout already uses 320 cores. For this problem size, further

speed-up is expected to be increasingly limited by communication, load balance, and input/output overhead. Because the revised coupling only changes the ownership and exchange of surface-flux variables and does not introduce additional horizontal interpolation, remapping, or new model components, the negligible overhead shown in Table 3 suggests that the revised heat-flux exchange does not materially affect computational performance under the configuration used in this study. A more complete scalability assessment for larger of higher-resolution CAPS configurations is left for future work.

3.2 Evaluation based on the MOSAiC observations

To provide a quantitative evaluation of CAPS against the MOSAiC observations, Figure 10 summarizes the correlation coefficient, normalized standard deviation, and normalized centered RMSE using Taylor diagrams, while Tables 4 and 5 list the corresponding bias and RMSE of Exp_FREE and Exp_NUD. Atmospheric variables are evaluated at altitudes of 1, 3, 5, 7, 9 km based on radiosonde observations, oceanic variables are evaluated at depths of 10, 20, 50, 75, 100 m based on CTD observations, and single-level sea-ice and surface-flux variables are evaluated at their corresponding observation levels. These quantitative metrics are discussed together with the time-series and profile comparisons in the following subsections.

3.2.1. Snow and ice mass balance

The evolutions of SIT and snow depth for the observations and the simulations along the MOSAiC drift are shown in Figure 11. For SIT (Fig. 11b), SIMBA shows ~1.0 m ice thickness at the beginning of December 2019 and reaches ~1.9 m at the beginning of June 2020. The

564 simulated SIT of Exp_FREE and Exp_NUD show some disagreement with that of the SIMBA
565 buoys, which is partly associated with that the simulations do not reproduce exactly the same
566 ice trajectory as the track of SIMBA buoys. Exp_FREE shows similar SIT as the SIMBA buoys
567 at the beginning of December 2019 and comparable thickening changes from December 2019
568 to February 2020. Afterwards, SIT in Exp_FREE shows early thinning changes relative to the
569 SIMBA buoys. On the other hand, SIT in Exp_NUD shows overall thickening evolutions,
570 which are relatively similar to those by the SIMBA buoys. Exp_NUD also shows thicker SIT
571 compared to the SIMBA buoys (~1.2 m vs. ~1.0 m, which still lies within the uncertainty range
572 of SIMBA) at the beginning of December 2019. For snow depth (Fig. 11a), snow depth
573 observed by the SIMBA buoys is near constant (~20 cm) from December 2019 to June 2020
574 and then decreases afterward. Both Exp_FREE and Exp_NUD can simulate the timing of snow
575 depth decreases. However, in contrast to the nearly constant snow depth observed from
576 December 2019 to May 2020, both experiments show a continuous increase in snow depth
577 during this period. Also, Exp_NUD shows relatively larger snow accumulation than
578 Exp_FREE. The quantitative metrics are consistent with these features. For SIT, Exp_NUD
579 shows a much higher correlation with SIMBA than Exp_FREE and reduces the bias/RMSE
580 from -0.38 m / 0.49 m in Exp_FREE to -0.05 m / 0.20 m in Exp_NUD (Tables 4–5). In contrast,
581 both experiments show comparable correlations for snow depth, but the normalized standard
582 deviation is larger than one, especially in Exp_NUD, indicating excessive snow-depth
583 variability associated with the simulated snow accumulation events (11a).

584 Similar to SIV budget averaged for the entire domain discussed in Section 3.1, the snow

585 and SIV budgets along the track of SIMBA buoys for Exp_FREE and Exp_NUD are shown in
586 Figure 12 to interpret the above-described simulated biases. Figure 12 indicates that the
587 evolutions of SIT (Fig. 11b), especially the SIT thinning, are primarily driven by basal melt for
588 both Exp_FREE and Exp_NUD. Exp_FREE shows larger basal melt and earlier increases in
589 basal melt than Exp_NUD (Figs. 12b, d). For snow depth, the thickening of snow depth in
590 Exp_FREE and Exp_NUD are associated with individual snowing events (i.e., spikes in snow
591 fall shown in Figs. 12a, c). Since snow volume budgets in Exp_FREE and Exp_NUD are well
592 correlated with the evolutions of snow depth shown in Fig. 11a, this indicates that the
593 discrepancy between the simulated snow depth and the SIMBA observations may be associated
594 with missing processes in the CICE model. Currently, ice thermodynamics in the CICE model
595 (Bitz and Lipscomb, 1999; Turner and Hunke, 2015) treat snow and ice as an integral, and
596 snow is not independently transported to other grid cells by surface wind.

597 **3.2.2. Surface atmospheric energy budget**

598 Figure 13 shows radiative and turbulent heat fluxes at the ice surface for the observations
599 and the simulations along the MOSAiC drift. For NetSW (Fig. 13a), Exp_FREE, Exp_NUD,
600 and the observations show similar evolution of NetSW from March to June 2020. Afterward,
601 both Exp_FREE and Exp_NUD simulate smaller peak of NetSW in mid-June 2020 with
602 underestimations of ~40 W/m^2 for both Exp_FREE and Exp_NUD compared with the
603 observations. For NetLW (Fig. 13b), Exp_FREE and Exp_NUD, show different periods with
604 smaller biases compared with the observations from November 2019 to June 2020. Afterward,
605 both Exp_FREE and Exp_NUD show overestimations (~15-25 W/m^2 for Exp_FREE, ~10-15

606 W/m^2 for Exp_NUD) of NetLW compared to the observed values. For turbulent heat fluxes
607 (Fig. 13c–d), both Exp_FREE and Exp_NUD show similar evolution of SH and LH, and the
608 simulated SH and LH are similar to the observations from November 2019 to February 2020.
609 Afterward, the simulated SH and LH begin to show biases compared with the observed SH and
610 LH, especially the simulated LH from May 2020 to June 2020. Both Exp_FREE and Exp_NUD
611 show different timings with smaller/larger biases in NetLW, SH, and LH compared to the
612 observed values, indicating the grid cell nearest to the locations of the observations in
613 Exp_FREE and Exp_NUD are experiencing different synoptic systems in the atmosphere
614 during the simulation period. The Taylor metrics further show that the radiative fluxes are better
615 constrained than the turbulent fluxes. NetSW and NetLW have relatively high correlations with
616 the observations in both experiments, whereas SH shows weak correlation and LH shows
617 strongly overestimated normalized standard deviation (Fig. 10b). The bias and RMSE statistics
618 indicate comparable overall surface-flux performance between Exp_FREE and Exp_NUD,
619 with Exp_NUD slightly reducing RMSE for NetLW and LH but increasing RMSE for NetSW
620 and SH (Tables 4–5). Therefore, spectral nudging applied above the boundary-layer height does
621 not lead to a uniform improvement in all ice-surface flux components along the MOSAiC drift.
622 Although Exp_FREE and Exp_NUD show biases in net radiative and turbulent heat fluxes, the
623 net heat fluxes over the ice surface, which is the major factor determining changes in ice
624 temperature, ice melt, and ice growth in CICE, show better agreement with the observational
625 values for both Exp_FREE and Exp_NUD due to bias cancellation (Fig. S5 in the supplement).

626 **3.2.3. Atmospheric profile**

627 Figure 14 shows the vertical profiles of atmosphere temperature and relative humidity
628 (RH) measured by radiosondes launched during the MOSAiC expedition, and the difference
629 between the observations and the experiments along the track of MOSAiC drift. For
630 atmospheric temperature profiles, Exp_FREE simulates profiles with biases oscillating
631 between warm and cold, and the magnitude of biases is larger from October 2019 to April 2020
632 (Fig. 14b) compared to the rest of periods. From December 2019 to April 2020, Exp_FREE
633 shows excessively warm biases, exceeding 10 °C above ~8 km altitude. In contrast to
634 Exp_FREE, Exp_NUD shows smaller temperature differences relative to the radiosonde
635 observations, with most differences confined within approximately ±10 °C (Fig. 14c). However,
636 the remaining non-zero differences indicate that constraining the simulated atmosphere toward
637 ERA5 does not eliminate all biases against the MOSAiC radiosondes. These residual
638 differences suggest that the radiosonde comparison is also influenced by uncertainties in the
639 large-scale atmospheric state used for nudging and by sub-grid-scale processes not fully
640 constrained by spectral nudging. Low-level temperature inversions are common features over
641 Arctic sea ice (e.g., Serreze et al., 1992; Devasthale et al., 2010), The inversion structures in
642 the radiosonde observations and all experiments are evaluated in Fig. S6. Exp_FREE
643 reproduces the frequent occurrence of low-level temperature inversions during the cold season,
644 but differs from the radiosondes in their timing and vertical distribution (Figs. S6a, c). With
645 spectral nudging applied, Exp_NUD shows a closer overall representation than Exp_FREE,
646 but still does not fully capture the observed inversion evolution (Figs. S6d). In addition,
647 Exp_FREE_OLD shows stronger inversions during the cold season compared with Exp_FREE,

indicting the inconsistency in heat-flux exchange induced by the original coupling approach (Fig. 6) alters the low-level temperature structure (Fig. S6b).

For RH profiles, Exp_FREE simulates mainly dryer profiles with intermittent wetter profiles relative to the radiosondes (Fig. 14e). These intermittent profiles are mainly wetter above ~500 m altitude. Below ~500 m altitude, these intermittent profiles are generally dryer compared to the radiosondes. Exp_NUD shows similar patterns in RH profiles (i.e., generally dryer, and intermittently wetter above ~500 m altitude) as Exp_FREE, but smaller differences relative to the observations (Fig. 14f). The quantitative metrics confirm that the nudged experiment is closer to the radiosonde profiles than Exp_FREE. For temperature, Exp_NUD shows higher correlations and smaller RMSEs than Exp_FREE at the evaluated altitude levels, and its normalized standard deviations are generally closer to the observations (Fig. 10c; Tables 4–5). RH remains more challenging in both experiments, although Exp_NUD also reduces the RMSE of RH relative to Exp_FREE. However, because Exp_NUD constrains the atmospheric state through spectral nudging, these improvements should be interpreted primarily as reduced large-scale atmospheric and synoptic biases, rather than as an isolated improvement of the model physical parameterizations.

The differences in temperature and RH profiles between Exp_FREE and Exp_NUD shown in Figure 14 are partly associated with the simulated synoptic systems compared with the observations. MOSAiC was characterized by anomalous high frequencies of storms relative to the period of 1979-2020 impacting the trajectory of MOSAiC drift (Liang et al., 2025). These storm events were associated with anomalous meteorological conditions during the MOSAiC

669 period such as anomalously warm conditions by storms during 16th to 20th November 2019,
670 and anomalously low sea level pressure condition by storms during 11th to 25th March 2020
671 (hereafter referred as STORM-1 and STORM-2; Rinke et al., 2021). The average mean sea
672 level pressure (MSLP), near-surface air temperature (T2), and 10 m wind fields (UV10) in
673 ERA5, Exp_FREE, and Exp_NUD for the period of STORM-1 and STORM-2 are shown in
674 Figure 15. The average temperature and RH profiles for Exp_FREE, Exp_NUD, and the
675 radiosondes are also shown in the supplement (Fig. S7) during both storm periods. During the
676 STORM-1 period, in ERA5, the averaged location of radiosondes (Fig. 15, white stars) is
677 positioned in the central Arctic encompassing by a low-pressure system (Fig. 15a). Exp_FREE
678 also simulates a low-pressure system with lower MSLP encompassing the averaged location of
679 radiosondes (Fig. 15b). The similarity of atmospheric circulations between ERA5 and
680 Exp_FREE near the averaged location of radiosondes results in similar average temperature
681 profiles from surface to 7 km altitude (Fig. S7). During the STORM-2 period, a low-pressure
682 system located over the Barents-Kara Seas encompasses the radiosondes in ERA5 (Fig. 15d)
683 while Exp_FREE shows a low-pressure system centered over the Greenland Sea and the
684 averaged location of radiosondes is positioned at the location with higher MSLP (Fig. 15e).
685 The atmospheric circulations and temperature fields in Exp_FREE result in the warm advection
686 from the North Atlantic to the location of MOSAiC during the STORM-2 period (Fig. 15k),
687 which partly contributes to the warmer profiles in Exp_FREE from surface to ~7 km altitude
688 (Figs. 15, S7b). Exp_FREE also shows enhanced warm biases above ~7 km altitude for both
689 STORM-1 and STORM-2 periods (Fig. S7a–b in the supplement). The temperature and wind

690 fields at 8 to 10 km altitude (Fig. S8 in the supplement) show that the warm bias in Exp_FREE
691 increases with altitude. This may be associated with biases from the stratosphere and the model
692 top boundary as suggested by Cassano et al. (2011). In contrast to Exp_FREE, the simulated
693 atmospheric circulations and temperature fields in Exp_NUD resemble those in ERA5 during
694 both storm periods (Fig. 15) corresponding to small temperature biases shown in the simulated
695 profiles (Figs. 14c, S7a–b). However, CAPS with the nudging scheme still faces challenges in
696 simulating RH conditions during the STORM-1 and STORM-2 periods (Fig. S7c–d). As shown
697 by Figures 14 and 15, the accuracy in simulating the synoptic conditions is crucial for CAPS
698 reproducing the observed vertical thermal structure in the Arctic. The results show that larger
699 biases in Exp_FREE from December 2019 to April 2020 described above (Fig. 14) are partly
700 associated with that Exp_FREE does not properly reproduce these synoptic systems during this
701 period. Liang et al. (2025) also show that the storm events impacting the MOSAiC site are
702 mostly concentrated in the ice growth period (November 2019 to March 2020).

703 **3.2.4. Oceanic profile**

704 Figure 16 shows the time-depth distributions of ocean temperature and salinity from the
705 CTD observations, and the corresponding differences between the simulations and
706 observations along the MOSAiC drift. For ocean temperature, both Exp_FREE and Exp_NUD
707 reproduce the overall cold upper-ocean conditions during most of the MOSAiC period, but
708 they show warm biases at different depths and periods (Fig. 16b–c). Before February 2020,
709 both experiments show slightly warmer temperatures by about 0.2-0.4 ˚C between 30 and 80
710 m. From March to June 2020, the positive temperature differences increase with depth, and the

711 simulations are about 0.5-1.0 °C warmer than the observations in the 60-100 m layer. Both
712 experiments also show slightly colder temperatures between 80 and 100 m before January 2020.
713 The quantitative metrics indicate that Exp_NUD reduces the ocean-temperature differences
714 relative to Exp_FREE. At evaluated depths of 10, 20, 50, 75, and 100 m, the temperature RMSE
715 decreases from 0.37-0.87 °C in Exp_FREE to 0.17-0.73 °C in Exp_NUD (Tables 4–5). The
716 Taylor diagram also shows that Exp_NUD generally has higher correlations and smaller
717 normalized centered RMSEs than Exp_FREE for ocean temperature, especially in the upper
718 50 m (Fig. 10d). Therefore, the improvement associated with the nudged atmospheric state is
719 more evident for ocean temperature than for salinity.

720 For salinity, both experiments show fresher upper-ocean biases before December 2019,
721 with differences of about 1.0-2.0 psu in the upper layer (Fig. 16e–f). Afterward, both
722 experiments show better agreement with the observed salinity, with differences generally
723 within ±0.25 psu in the upper 40 m, and this better agreement extends downward to 100 m until
724 May 2020. However, the quantitative metrics indicate that the salinity improvement is not
725 systematic. Although Exp_NUD shows higher correlations at several depths and slightly
726 smaller normalized centered RMSEs below 20 m, it also shows stronger fresh biases and
727 slightly larger full RMSEs than Exp_FREE at the evaluated depths (Tables 4–5). Thus, the
728 salinity biases appear less sensitive to the atmospheric nudging than the temperature biases
729 along the MOSAiC drift.

730 After June 2020, the significant differences in oceanic temperature and salinity between
731 the simulations and observations are associated with the simulated SIC and upper-ocean

thermal structure along the track of CTD buoys. Both Exp_FREE and Exp_NUD show warm biases around July 2020 in the 10-100 m layer, and warm biases in Exp_FREE, exceeding 1.5 °C, are larger than those in Exp_NUD, which are around 0.5 °C. These warm biases correspond to simulated SIC values below 0.9, while the observations still indicate nearly complete ice cover (Fig. S9 in the supplement). The spatial distribution of temperature and salinity at 10, 50, and 100 m depth on July 1st, 2020 further indicates that these biases are associated with simulated Atlantic inflow structure (Fig. S10 in the supplement).

4. Conclusions and Discussions

This study introduces an improved version of Coupled Arctic Prediction System (CAPS) that conserves surface heat fluxes between the atmosphere and ocean-sea ice components. A set of pan-Arctic numerical experiments covering the entire MOSAiC expedition have been conducted for assessing the improvement in simulating Arctic sea-ice conditions contributed by the improved coupling approach, and for the comprehensive evaluation of improved CAPS in simulating Arctic atmosphere–sea-ice–ocean coupled system against the MOSAiC observations.

The results show that the inconsistency in heat-flux exchange between the atmosphere and ocean-sea ice components shown in the previous version of CAPS has been significantly minimized with the improved coupling approach, and the simulated Arctic sea-ice conditions with the improved CAPS are more comparable to satellite-based sea-ice observations than those with the previous version of CAPS. In this study, the simulated sea-ice conditions in the free-running experiment are sensitive to the choices of physics options across the atmospheric,

753 sea-ice, ocean model components. Simulations conducted with the improved CAPS choosing
754 the same physics options used in the previous version of CAPS (e.g., Yang et al., 2022) can
755 result in the underperformance of the simulated sea-ice conditions (not shown). This indicates
756 further investigations of physical processes in CAPS are required to improve the performance
757 of CAPS. Firstly, CAPS faces challenges to simulate surface heat flux budget over the ice
758 surface. Liu et al. (2024) found that the atmospheric boundary layer observed during MOSAiC
759 can be categorized into a surface inversion type and an elevated inversion type, and the
760 enhanced non-local effects associated with a surface inversion type pose difficulties on
761 similarity theory-based parametrizations to simulate surface sensible heat fluxes. Secondly,
762 CAPS does not well reproduce the temperature inversions compared with the radiosonde
763 observations. The strong temperature inversions in wintertime Arctic have important effects on
764 the magnitude of downward longwave radiation near the surface (Bintanja et al., 2011). The
765 simulated downward longwave radiation is shown to be associated with the boundary layer
766 stability (e.g., Jozef et al., 2024). Thirdly, surface radiative heat fluxes are regulated by clouds
767 (e.g., Curry et al., 1996; Shupe and Intrieri, 2004). However, it is still challenging for CAPS to
768 properly reproduce liquid water content (LWC) and ice water content (IWC) associated with
769 the frequent occurrence of Arctic mixed-phase clouds and their associated radiative impacts
770 (e.g., Tan et al., 2023) during the MOSAiC expedition. Here, an additional experiment is
771 conducted for the STORM-1 period with high-frequency outputs for cloud properties, and the
772 calculated LWC and IWC compared with the MOSAiC observations are shown in Figure 17.
773 Generally, CAPS strongly underestimates both LWC and IWC during the STORM-1 period in

774 terms of the occurrence and vertical distribution, which corresponds to the simulated dryer
775 atmospheric profiles (Fig. 14). The underestimations of LWC and IWC are associated with the
776 treatment in the microphysics and atmospheric boundary layer schemes (e.g., Arteaga et al.,
777 2024; Sedlar et al., 2020). Arteaga et al. (2024) also suggest that increases in the cloud
778 condensation nuclei and droplet number concentrations in the microphysics schemes can have
779 impacts on the simulated LWC and IWC. Furthermore, it is essential to increase model
780 resolution both horizontally and vertically to properly simulate the phase heterogeneity in
781 Arctic clouds (e.g., Dammann et al., 2025), which demands more computational resources for
782 high-resolution simulations. Regardless of the challenges posed to CAPS, the consistent energy
783 exchange between the atmosphere and ocean–sea ice components in CAPS provides a solid
784 foundation for future improvements in the representation of physical processes, especially for
785 processes related to surface heat flux calculations.

786 The improved coupling reduces the interfacial heat-flux residuals and improves the
787 simulated sea-ice evolution relative the original coupling approach in the free-running
788 configuration. In addition to this coupling-focused comparison, the MOSAiC evaluation shows
789 that the constrained-atmosphere experiment, Exp_NUD, agrees more closely with observations
790 in several quantitative metrics, especially for radiosonde temperature/RH profiles and ocean
791 temperature. However, this improved agreement reflects the combined effect of the revised
792 coupled model and the imposed large-scale atmospheric constraint. Moreover, non-negligible
793 biases remain in Exp_NUD, indicating that spectral nudging can reduced errors associated with
794 large-scale atmospheric evolution but cannot fully compensate for biases in physical

795 parameterizations, coupled surface exchange, or the reanalysis fields used for nudging.
796 Therefore, Exp_NUD is used as a sensitivity experiment to examine how the coupled system
797 responds when large-scale atmospheric state is constrained, rather than as evidence that the
798 revised coupling or model physics alone removes the remaining biases.

799 Because Exp_NUD applies spectral nudging above the boundary-layer height, it
800 represents a relatively strongly constrained experiment. To assess whether the MOSAiC
801 evaluation depends on the vertical extent and strength of this constraint, we conducted two
802 additional sensitivity experiments. Exp_NUD_UPD applies spectral nudging only to the upper
803 25 of the 50 WRF model levels (approximately above 6.7 km altitude), with a 10-level
804 transition zone from zero to the full nudging weight of 0.0003 s^{-1}, following a design similar
805 to Cassano et al. (2011), whereas Exp_NUD_UPW uses the same vertical design but reduces
806 the nudging weight by one order of magnitude (Glisan et al., 2013). The additional nudging
807 experiments further indicate that the MOSAiC evaluation remains sensitive to the nudging
808 configuration. In the radiosonde comparison, Exp_NUD_UPD and Exp_NUD_UPW both
809 reduce the large temperature departures seen in the free-running atmosphere, but residual
810 temperature and RH differences remain throughout the troposphere, especially in the lower
811 atmosphere and during late summer (Fig. S11). The snow/sea-ice comparison also shows that
812 changing the vertical extent and strength of nudging modifies snow accumulation and melt
813 timing, while the simulated SIT remains within the broad observational uncertainty (Fig. S12).
814 Surface fluxes are likewise sensitive to the nudging setup, in particular turbulent heat fluxes
815 during spring and summer (Fig. S13).

In this study, the implementation of our revised coupling approach is based on the shared horizontal grid between the atmosphere component and the ocean-sea ice component. For applications that require higher resolution (e.g., sea-ice linear kinematic features, ocean eddies in polar oceans), both the atmosphere model and the ocean-sea ice model have to increase their resolutions to the same grid in our current coupling approach, which may be computationally unrealistic for the atmosphere component. CAPS does have the capability for the atmosphere component and the ocean-sea ice component using different grids through the interpolation weightings generated by the Earth System Modeling Framework (ESMF). However, the interpolation is mask-to-mask basis in CAPS, i.e., a smaller ocean-sea ice grid cell may represent a larger ocean mask (especially near the complex topography) in the atmosphere component. That is, the spatial heterogeneity of the surface types (i.e., the mixture of land, ocean, and sea ice) within a larger atmosphere grid cell is not properly treated. This will lead to less flux consistency between the atmosphere component and the ocean-sea ice component. Recently, a regional modeling system developed by Karsten et al. (2024), which applies a flux coupling approach (e.g., Balaji et al., 2006) on an exchange grid, demonstrates the future direction of improving our coupling approach for wider applications. With the flux coupling approach on an exchange grid, a locally consistent treatment of the surface fluxes between model components with independent grids is achievable.

Code and data availability:

This study uses publicly available sea-ice satellite observations, atmosphere, and ocean reanalysis from the original data providers: NSIDC-0051 sea-ice concentration (https://nsidc.org/data/nsidc-0051/versions/2; last access: 30 Nov 2025), CS2SMOS sea-ice thickness (https://data.meereisportal.de/relaunch/CS2SMOS.php; last access: 30 Nov 2025), PIOMAS sea-ice thickness (https://psc.apl.uw.edu/research/projects/arctic-sea-ice-volume-anomaly/data/; last access: 30 Nov 2025), ERA5 atmospheric reanalysis (https://cds.climate.copernicus.eu/datasets/; last access: 30 Nov 2025), and CMEMS GREP ocean and sea-ice products (https://data.marine.copernicus.eu/products; last access: 30 Nov 2025). MOSAiC datasets were obtained from the following DOIs: radiosonde data (Maturilli et al., 2022; https://doi.pangaea.de/10.1594/PANGAEA.943870), cloud microphysics (Shupe, 2022; https://doi.org/10.5439/1871015), surface fluxes (Cox et al., 2023a–d; https://doi.org/10.18739/A2PV6B83F; https://doi.org/10.18739/A2FF3M18K; https://doi.org/10.18739/A25X25F0P; https://doi.org/10.18739/A2XD0R00S), CTD data (Hoppmann et al., 2022; https://doi.pangaea.de/10.1594/PANGAEA.940271), and SIMBA data (Lei et al., 2021; https://doi.org/10.1594/PANGAEA.938267).

To ensure full and long-term reproducibility, the exact evaluation datasets used in this study (including NSIDC-0051, CS2SMOS, PIOMAS sea ice data, and the processed MOSAiC datasets used for evaluation) are archived in Zenodo repository: https://doi.org/10.5281/zenodo.18764432 (Yang, 2026a). The exact model version used to produce the results is archived in Zenodo repository: https://doi.org/10.5281/zenodo.18308943 (Yang, 2026b). The pan-Arctic simulation outputs analyzed in this study are archived in Zenodo repository: https://doi.org/10.5281/zenodo.18308549 (Yang, 2026c).

Author contributions: CYY implemented the revised coupling approach in CAPS,

conducted numerical experiments, and wrote the original manuscript. FG performed the evaluation based on the MOSAiC data. CYY and JL were responsible for the conceptualization of this study. CYY, FG, JL, and AR were responsible for the revisions of the manuscript. All co-authors reviewed and commented on the final version of the manuscript.

Competing interests: The authors declare that they have no conflict of interest.

Acknowledgements: This research is supported by the National Natural Science Foundation of China (42376237), and the Innovation Group Project of Southern Marine Science and Engineering Guangdong Laboratory (Zhuhai) (311021008).

5. References

Arteaga, D., Planche, C., Tridon, F., Dupuy, R., Baudoux, A., Banson, S., Baray, J.-L., Mioche, G., Ehrlich, A., Mech, M., Mertes, S., Wendisch, M., Wobrock, W., and Jourdan, O.: Arctic mixed-phase clouds simulated by the WRF model: Comparisons with ACLOUD radar and in situ airborne observations and sensitivity of microphysics properties, *Atmos. Res.*, 307, 107471, https://doi.org/10.1016/j.atmosres.2024.107471, 2024.

Balaji, V., Anderson, J., Held, I., Winton, M., Durachta, J., Malyshev, S., and Stouffer, R. J.: The Exchange Grid: a mechanism for data exchange between Earth System components on independent grids, in: Parallel computational fluid dynamics 2005, 179–186, Elsevier, https://doi.org/10.1016/B978-044452206-1/50021-5, 2006.

Bintanja, R., Graversen, R. and Hazeleger, W.: Arctic winter warming amplified by the thermal inversion and consequent low infrared cooling to space. *Nat. Geosci.*, 4, 758–761, https://doi.org/10.1038/ngeo1285, 2011.

Bitz, C. M. and Lipscomb, W. H.: An energy-conserving thermodynamic sea ice model for climate study. *J. Geophys. Res.-Oceans*, 104, 15669–15677, https://doi.org/10.1029/1999JC900100, 1999.

Bliss, A. C., Hutchings, J. K., and Watkins, D. M.: Sea ice drift tracks from autonomous buoys in the MOSAiC Distributed Network, *Sci. Data*, 10, 403, https://doi.org/10.1038/s41597-023-02311-y, 2023.

Briegleb, B. P. and Light, B.: A Delta-Eddington multiple scattering parameterization for solar radiation in the sea ice component of the Community Climate System Model. (No. NCAR/TN-472+STR). *University Corporation for Atmospheric Research*, https://doi.org/10.5065/D6B27S71, 2007.

Cassano, J. J., Higgins, M. E., and Seefeldt, M. W.: Performance of the Weather Research and Forecasting Model for Month-Long Pan-Arctic Simulations. *Mon. Wea. Rev.*, 139, 11, 3469-3488, https://doi.org/10.1175/MWR-D-10-05065.1, 2011.

Chen, F. and Dudhia, J.: Coupling an advanced land surface–hydrology model with the Penn State–NCAR MM5 modeling system. Part I: Model implementation and sensitivity. *Mon. Wea. Rev.*, 129, 569–585, https://doi.org/10.1175/1520-0493(2001)129<0569:CAALSH>2.0.CO;2, 2001.

Cocetta, F., Zampieri, L., Selivanova, J., and Iovino, D.: Assessing the representation of Arctic sea ice and the marginal ice zone in ocean–sea ice reanalyses, *The Cryosphere*, 18, 4687–4702, https://doi.org/10.5194/tc-18-4687-2024, 2024.

Cohen, J., Screen, J. A., Furtado, J. C., Barlow, M., Whittleston, D., Coumou, D., Francis, J., Dethloff, K., Entekhabi, D., Overland, J., and Jones, J.: Recent Arctic amplification and extreme mid-latitude weather. *Nat. Geosci.*, 7, 627–637, https://doi.org/10.1038/ngeo2234, 2014.

Cohen, J., Zhang, X., Francis, J., Jung, T., Kwok, R., Overland, J., Ballinger, T. J., Bhatt, U. S., Chen, H. W., Coumou, D., Feldstein, S., Gu, H., Handorf, D., Henderson, G., Ionita, M., Kretschmer, M., Laliberte, F., Lee. S, Linderholm, H. W., Maslowski, W., Peings, Y., Pfeiffer, K., Rigor, I., Semmler, T., Stroeve, J., Taylor, P. C., Vavrus, S., Vihma, T., Wang, S., Wendisch, M., Wu, Y., and Yoon, J.: Divergent consensuses on Arctic amplification influence on midlatitude severe winter weather. *Nat. Clim. Chang.*, 10, 20–29, https://doi.org/10.1038/s41558-019-0662-y, 2020.

Cox, C. J., Gallagher, M., Shupe, M., Persson, O., Blomquist, B., Grachev, A., Riihimaki, L., Kutchenreiter, M., Morris, V., Solomon, A., Brooks, I., Costa, D., Gottas, D., Hutchings, J., Osborn, J., Morris, S., Preusser, A., and Uttal, T.: Met City meteorological and surface flux measurements (Level 3 Final), Multidisciplinary Drifting Observatory for the Study of Arctic Climate (MOSAiC), central Arctic, October 2019 – September 2020. *Arctic Data Center [data set]*, https://doi.org/10.18739/A2PV6B83F, 2023a.

Cox, C. J., Gallagher, M., Shupe, M., Persson, O., Blomquist, B., Grachev, A., Riihimaki, L., Kutchenreiter, M., Morris, V., Solomon, A., Brooks, I., Costa, D., Gottas, D., Hutchings, J., Osborn, J., Morris, S., Preusser, A., and Uttal, T.: Atmospheric Surface Flux Station

#30 measurements (Level 3 Final), Multidisciplinary Drifting Observatory for the Study of Arctic Climate (MOSAiC), central Arctic, October 2019 – September 2020. *Arctic Data Center [data set]*, https://doi.org/10.18739/A2FF3M18K, 2023b.

Cox, C. J., Gallagher, M., Shupe, M., Persson, O., Blomquist, B., Grachev, A., Riihimaki, L., Kutchenreiter, M., Morris, V., Solomon, A., Brooks, I., Costa, D., Gottas, D., Hutchings, J., Osborn, J., Morris, S., Preusser, A., and Uttal, T.: Atmospheric Surface Flux Station #40 measurements (Level 3 Final), Multidisciplinary Drifting Observatory for the Study of Arctic Climate (MOSAiC), central Arctic, October 2019 – September 2020. *Arctic Data Center [data set]*, https://doi.org/10.18739/A25X25F0P, 2023c.

Cox, C. J., Gallagher, M., Shupe, M., Persson, O., Blomquist, B., Grachev, A., Riihimaki, L., Kutchenreiter, M., Morris, V., Solomon, A., Brooks, I., Costa, D., Gottas, D., Hutchings, J., Osborn, J., Morris, S., Preusser, A., and Uttal, T.: Atmospheric Surface Flux Station #50 measurements (Level 3 Final), Multidisciplinary Drifting Observatory for the Study of Arctic Climate (MOSAiC), central Arctic, October 2019 – September 2020. *Arctic Data Center [data set]*, https://doi.org/10.18739/A2XD0R00S, 2023d.

Craig, A., Valcke, S., and Coquart, L.: Development and performance of a new version of the OASIS coupler, OASIS3-MCT_3.0, *Geosci. Model Dev.*, 10, 3297–3308, https://doi.org/10.5194/gmd-10-3297-2017, 2017.

Curry, J. A., Schramm, J. L., Rossow, W. B., and Randall, D.: Overview of Arctic Cloud and Radiation Characteristics, *J. Climate*, 9, 1731–1764, https://doi.org/10.1175/1520-0442(1996)009<1731:OOACAR>2.0.CO;2, 1996.

Dammann, S. L.-S., Schäfer, B., David, R. O., and Storelvmo, T.: Observations and model simulations of phase heterogeneity in Arctic clouds. *J. of Geophys. Res.-Atmos.*, 130, e2024JD042714. https://doi.org/10.1029/2024JD042714, 2025.

Danabasoglu, G., Lamarque, J.-F., Bacmeister, J., Bailey, D. A., DuVivier, A. K., Edwards, J., Emmons, L. K., Fasullo, J., Garcia, R., Gettelman, A., Hannay, C., Holland, M. M., Large, W. G., Lauritzen, P. H., Lawrence, D. M., Lenaerts, J. T. M., Lindsay, K., Lipscomb, W.

H., Mills, M. J., Neale, R., Oleson, K. W., Otto-Bliesner, B., Phillips, A. S., Sacks, W., Tilmes, S., van Kampenhout, L., Vertenstein, M., Bertini, A., Dennis, J., Deser, C., Fischer, C., Fox-Kemper, B., Kay, J. E., Kinnison, D., Kushner, P. J., Larson, V. E., Long, M. C., Mickelson, S., Moore, J. K., Nienhouse, E., Polvani, L., Rasch, P. J., and Strand, W. G.: The Community Earth System Model Version 2 (CESM2). *J. Adv. Model. Earth Sy.*, 12, e2019MS001916. https://doi.org/10.1029/2019MS001916, 2020.

Deng, J., and Dai, A.: Sea ice–air interactions amplify multidecadal variability in the North Atlantic and Arctic region. *Nat. Commun.*, 13, 2100, https://doi.org/10.1038/s41467-022-29810-7, 2022.

Deng, J., and Dai, A.: Arctic sea ice–air interactions weaken El Niño–Southern Oscillation. *Sci. Adv.*, 10, eadk3990, https://doi.org/10.1126/sciadv.adk3990, 2024

Devasthale, A., Willén, U., Karlsson, K.-G., and Jones, C. G.: Quantifying the clear-sky temperature inversion frequency and strength over the Arctic Ocean during summer and winter seasons from AIRS profiles, *Atmos. Chem. Phys.*, 10, 5565–5572, https://doi.org/10.5194/acp-10-5565-2010, 2010.

DiGirolamo, N. E., Parkinson, C. L., Cavalieri, D. J., Gloersen, P., and Zwally, H. J.: updated yearly. Sea Ice Concentrations from Nimbus-7 SMMR and DMSP SSM/I-SSMIS Passive Microwave Data, Version 2. Boulder, Colorado USA, *NASA National Snow and Ice Data Center Distributed Active Archive Center [data set]*, https://doi.org/10.5067/MPYG15WAA4WX, 2022.

Durski, S. M., Glenn, S. M., and Haidvogel, D. B.: Vertical mixing schemes in the coastal ocean: Comparison of the level 2.5 Mellor-Yamada scheme with an enhanced version of the K profile parameterization, *J. Geophys. Res.*, 109, C01015, https://doi.org/10.1029/2002JC001702, 2004.

Fairall, C. W., Bradley, E. F., Hare, J. E., Grachev, A. A., and Edson, J. B.: Bulk Parameterization of Air–Sea Fluxes: Updates and Verification for the COARE Algorithm.

977 *J. Climate*, 16(4), 571-591. https://doi.org/10.1175/1520-
978 0442(2003)016<0571:BPOASF>2.0.CO;2, 2003.
979 Freitas, S. R., Grell, G. A., Molod, A., Thompson, M. A., Putman, W. M., Santos e Silva, C.
980 M. and Souza, E. P.: Assessing the Grell–Freitas convection parameterization in the
981 NASA GEOS modeling system. *J. Adv. Model. Earth Syst.*, 10, 1266–1289,
982 https://doi.org/10.1029/2017MS001251, 2018.
983 Giles, K. A, Laxon, S. W., Ridout, A. L., Wingham, D. J., and Bacon, S.: Western Arctic Ocean
984 freshwater storage increased by wind-driven spin-up of the Beaufort Gyre. *Nat. Geosci.*,
985 5, 194–197, https://doi.org/10.1038/ngeo1379, 2012.
986 Glisan, J. M., Gutowski, W. J., Cassano, J. J., and Higgins, M. E.: Effects of Spectral Nudging
987 in WRF on Arctic Temperature and Precipitation Simulations. *J. Climate*, 26, 3985–3999,
988 https://doi.org/10.1175/JCLI-D-12-00318.1, 2013.
989 Goessling, H. F., Tietsche, S., Day, J. J., Hawkins, E., and Jung, T.: Predictability of the Arctic
990 sea ice edge, *Geophys. Res. Lett.*, 43, 1642–1650, https://doi.org/10.1002/2015GL067232,
991 2016.
992 Guemas, V., Blanchard-Wrigglesworth, E., Chevallier, M., Day, J. J., Déqué, M., Doblas-Reyes,
993 F. J., Fučkar, N. S., Germe, A., Hawkins, E., Keeley, S., Koenigk, T., Salas y Mélia, D.
994 and Tietsche, S.: A review on Arctic sea-ice predictability and prediction on seasonal to
995 decadal time-scales. *Q. J. R. Meteorol. Soc.*, 142: 546-561.
996 https://doi.org/10.1002/qj.2401, 2016.
997 Gutowski Jr., W. J., Giorgi, F., Timbal, B., Frigon, A., Jacob, D., Kang, H.-S., Raghavan, K.,
998 Lee, B., Lennard, C., Nikulin, G., O'Rourke, E., Rixen, M., Solman, S., Stephenson, T.,
999 and Tangang, F.: WCRP COordinated Regional Downscaling EXperiment (CORDEX): a
1000 diagnostic MIP for CMIP6, *Geosci. Model Dev.*, 9, 4087–4095,
1001 https://doi.org/10.5194/gmd-9-4087-2016, 2016.
1002 Haas, C.: Sea ice thickness distribution, in: Sea Ice, D. N. Thomas (Ed.).
1003 https://doi.org/10.1002/9781118778371.ch2, 2017.

1004 Hersbach, H., Bell, B., Berrisford, P., Biavati, G., Horányi, A., Muñoz Sabater, J., Nicolas, J.,
1005 Peubey, C., Radu, R., Rozum, I., Schepers, D., Simmons, A., Soci, C., Dee, D., Thépaut,
1006 J-N.: ERA5 hourly data on single levels from 1940 to present, *Copernicus Climate*
1007 *Change Service (C3S) Climate Data Store (CDS) [data set]*,
1008 https://doi.org/10.24381/cds.adbb2d47, 2023.
1009 Hines, K. M., Bromwich, D. H., Bai, L., Bitz, C. M., Powers, J. G., and Manning, K. W.: Sea
1010 Ice Enhancements to Polar WRF. *Mon. Wea. Rev.*, 143, 2363–2385,
1011 https://doi.org/10.1175/MWR-D-14-00344.1, 2015.
1012 Holland, M. M., and Bitz, C. M.: Polar amplification of climate change in coupled models.
1013 *Clim. Dyn.*, 21, 221–232, https://doi.org/10.1007/s00382-003-0332-6, 2003.
1014 Hoppmann, M., Kuznetsov, I., Fang, Y.-C., Rabe, B.: Processed data of CTD buoys 2019O1 to
1015 2019O8 as part of the MOSAiC Distributed Network, *PANGAEA [data set]*,
1016 https://doi.org/10.1594/PANGAEA.940320, 2022.
1017 Hunke, E. C. and Dukowicz, J. K.: An elastic-viscous-plastic model for sea ice dynamics. *J.*
1018 *Phys. Oceanogr.*, 27, 1849–67, https://doi.org/10.1175/1520-
1019 0485(1997)027<1849:AEVPMF>2.0.CO;2, 1997.
1020 Hunke, E. C., Hebert, D. A., and Lecomte, O.: Level-ice melt ponds in the Los Alamos Sea Ice
1021 Model, CICE. *Ocean Model.*, 71, 26–42, https://doi.org/10.1016/j.ocemod.2012.11.008,
1022 2013.
1023 Huntemann, M., Heygster, G., Kaleschke, L., Krumpen, T., Makynen, M., and Drusch, M.:
1024 Empirical sea ice thickness retrieval during the freeze-up period from SMOS high incident
1025 angle observations, *The Cryosphere*, 8, 439–451, https://doi.org/10.5194/tc-8-439-2014,
1026 2014.
1027 Iacono, M. J., Delamere, J. S., Mlawer, E. J., Shephard, M. W., Clough, S. A., and Collins, W.
1028 D.: Radiative forcing by long-lived greenhouse gases: Calculations with the AER radiative
1029 transfer models, *J. Geophys. Res.*, 113, D13103, https://doi.org/10.1029/2008JD009944,
1030 2008.

1031 Irving, D., Hobbs, W., Church, J., and Zika, J.: A Mass and Energy Conservation Analysis of
1032 Drift in the CMIP6 Ensemble. *J. Climate*, 34, 3157–3170, https://doi.org/10.1175/JCLI-
1033 D-20-0281.1, 2021.
1034 Jordan, R. E., Andreas, E. L., and Makshtas, A. P.: Heat budget of snow-covered sea ice at
1035 North Pole 4, *J. Geophys. Res.-Oceans*, 104(C4), 7785–7806,
1036 http://doi.org/10.1029/1999JC900011, 1999.
1037 Jozef, G., Cassano, J. J., Solomon, A., Intrieri, J., Boer, G.: Evaluation of the Coupled Arctic
1038 Forecast System's representation of the Arctic atmospheric boundary layer vertical
1039 structure during MOSAiC. *Elem. Sci. Anthropocene*, 12 (1): 00136,
1040 https://doi.org/10.1525/elementa.2023.00136, 2024.
1041 Kacimi, S. and Kwok, R.: Two Decades of Arctic Sea-Ice Thickness from Satellite Altimeters:
1042 Retrieval Approaches and Record of Changes (2003–2023). *Remote Sens.*, 16, 2983.
1043 https://doi.org/10.3390/rs16162983, 2024.
1044 Karsten, S., Radtke, H., Gröger, M., Ho-Hagemann, H. T. M., Mashayekh, H., Neumann, T.,
1045 and Meier, H. E. M.: Flux coupling approach on an exchange grid for the IOW Earth
1046 System Model (version 1.04.00) of the Baltic Sea region, *Geosci. Model Dev.*, 17, 1689–
1047 1708, https://doi.org/10.5194/gmd-17-1689-2024, 2024.
1048 Knust, R.: Polar research and supply vessel POLARSTERN operated by the Alfred-Wegener-
1049 Institute. *J. Large-Scale Res. Facil.*, 3, https://doi.org/10.17815/jlsrf-3-163, 2017.
1050 Konda, M., Imasato, N., Nishi, K., and Toda, T.: Measurement of the sea surface emissivity. *J.*
1051 *Oceanogr.*, 50(1), 17–30, https://doi.org/10.1007/BF02233853, 1994.
1052 Large, W. G., McWilliams, J. C., and Doney, S. C.: Oceanic vertical mixing: A review and a
1053 model with a nonlocal boundary layer parameterization. *Rev. Geophys.*, 32(4), 363–403,
1054 https://doi.org/10.1029/94RG01872, 1994.
1055 Larson, J., Jocab, R., and Ong, E.: The Model Coupling Toolkit: A New Fortran90 Toolkit for
1056 Building Multiphysics Parallel Coupled Models, *Int. J. High Perform. Comput. Appl.*,
1057 19(3), 277–292, https://doi.org/10.1177/1094342005056115, 2005.

1058 Liang, Y., Lei, R., Bi, H., and Chen, X.: Response of changes in sea ice thickness to cyclones:
1059 new insights from the MOSAiC expedition. *J. Climate*, 38, 6709–6726,
1060 https://doi.org/10.1175/JCLI-D-24-0765.1, 2025.
1061 Liepert, B. G., and Previdi, M.: Inter-model variability and biases of the global water cycle in
1062 CMIP3 coupled climate models. *Environ. Res. Lett.*, 7, 014006,
1063 https://doi.org/10.1088/1748-9326/7/1/014006, 2012.
1064 Liu, C., Yang, Q., Gao, Z., Shupe, M. D., Han, B., Zhang, H., Peng, S., Xi, X., and Chen, D.:
1065 The role of non-local effects on surface sensible heat flux under different types of thermal
1066 structures over the Arctic sea-ice surface. *Geophys. Res. Lett.*, 51, e2023GL106753.
1067 https://doi.org/10.1029/2023GL106753, 2024.
1068 Liu, J., Song, M., Zhu, Z., Horton, R. M., Hu, Y., and Xie, S.-P.: Arctic sea-ice loss is projected
1069 to lead to more frequent strong El Niño events. *Nat. Commun.*, 13, 4952,
1070 https://doi.org/10.1038/s41467-022-32705-2, 2022.
1071 Lei, R., Cheng, B., Hoppmann, M., and Zuo, G.: An overview of SIMBA buoys deployed in
1072 the Arctic Ocean during the Legs 1a, 1, and 3 of the MOSAiC campaign in 2019-2020,
1073 *PANGAEA [data set]*, https://doi.org/10.1594/PANGAEA.938267, 2021.
1074 Lei, R., Cheng, B., Hoppmann, M., Zhang, F., Zuo, G., Hutchings, J. K., Lin, L., Lan, M., Wang,
1075 H., Regnery, J., Krumpen, T., Haapala, J., Rabe, B., Perovich, D. K., and Nicolaus, M.:
1076 Seasonality and timing of sea ice mass balance and heat fluxes in the Arctic transpolar
1077 drift during 2019–2020. *Elem. Sci. Anthropocene*, 10, 89.
1078 https://doi.org/10.1525/elementa.2021.000089, 2022.
1079 Leonard, B. and Mokhtari, S.: ULTRA-SHARP nonoscillatory convection schemes for high-
1080 speed steady multidimensional flow, *NASA Technical Memorandum 102568*, ICOMP-90-
1081 12, 54 pp., https://ntrs.nasa.gov/citations/19900012254 (last access: 30 Nov 2025), 1990.
1082 Lucarini, V., and Ragone, F.: Energetics of climate models: Net energy balance and meridional
1083 enthalpy transport. *Rev. Geophys.*, 49, RG1001, https://doi.org/10.1029/2009RG000323,
1084 2011.

Malyarenko, A., Gossart, A., Sun, R., and Krapp, M.: Conservation of heat and mass in P-SKRIPS version 1: the coupled atmosphere–ice–ocean model of the Ross Sea, *Geosci. Model Dev.*, 16, 3355–3373, https://doi.org/10.5194/gmd-16-3355-2023, 2023.

Maturilli, M., Sommer, M., Holdridge, D. J., Dahlke, S., Graeser, J., Sommerfeld, A., Jaiser, R., Deckelmann, H., and Schulz, A.: MOSAiC radiosonde data (level 3), *PANGAEA [data set]*, https://doi.org/10.1594/PANGAEA.943870, 2022.

Maykut, G. A. and McPhee. M. G.: Solar heating of the Arctic mixed layer, *J. Geophys. Res.-Oceans*, 100, 24691–24703, http://doi.org/10.1029/95JC02554, 1995.

Meier, W. N., Petty, A., Hendricks, S., Bliss, A., Kaleschke, L., Divine, D., Farrell, S., Gerland, S., Perovich, D., Ricker, R., Tian-Kunze, X., and Webster M.: Sea Ice. *Arctic Report Card 2024, Moon*, T. A., Druckenmiller, M. L., and Thoman, R. L., Eds., https://doi.org/10.25923/aksk-7p66, 2024.

Morrison, H., Thompson, G., and Tatarskii, V.: Impact of Cloud Microphysics on the Development of Trailing Stratiform Precipitation in a Simulated Squall Line: Comparison of One– and Two–Moment Schemes. *Mon. Wea. Rev.*, 137, 991-1007. https://doi.org/10.1175/2008MWR2556.1, 2009.

Nakanishi, M., and Niino., H.: Development of an improved turbulence closure model for the atmospheric boundary layer. *J. Meteor. Soc. Japan*, 87, 895–912, https://doi.org/10.2151/jmsj.87.895, 2009.

Nicolaus, M., Perovich, D., Spreen, G., Granskog, M., Albedyll, L., Angelopoulos, M., Anhaus, P., Arndt, S., Belter, H., Bessonov, V., Birnbaum, G., Brauchle, J., Calmer, R., Cardellach, E., Cheng, B., Clemens-Sewall, D., Dadic, R., Damm, E., de Boer, G., Demir, O., Dethloff, K., Divine, D., Fong, A., Fons, S., Frey, M., Fuchs, N., Gabarró, C., Gerland, S., Goessling, H., Gradinger, R., Haapala, J., Haas, C., Hamilton, J., Hannula, H.-R., Hendricks, S., Herber, A., Heuzé, C., Hoppmann, M., Høyland, K., Huntemann, M., Hutchings, J., Hwang, B., Itkin, P., Jacobi, H.-W., Jaggi, M., Jutila, A., Kaleschke, L., Katlein, C., Kolabutin, N., Krampe, D., Kristensen, S., Krumpen, T., Kurtz, N., Lampert, A., Lange,

B., Lei, R., Light, B., Linhardt, F., Liston, G., Loose, B., Macfarlane, A., Mahmud, M., Matero, I., Maus, S., Morgenstern, A., Naderpour, R., Nandan, V., Niubom, A., Oggier, M., Oppelt, N., Pätzold, F., Perron, C., Petrovsky, T., Pirazzini, R., Polashenski, C., Rabe, B., Raphael, I., Regnery, J., Rex, M., Ricker, R., Riemann-Campe, K., Rinke, A., Rohde, J., Salganik, E., Scharien, R., Schiller, M., Schneebeli, M., Semmling, M., Shimanchuk, E., Shupe, M., Smith, M., Smolyanitsky, V., Sokolov, V., Stanton, T., Stroeve, J., Thielke, L., Timofeeva, A., Tonboe, R., Tavri, A., Tsamados, M., Wagner, D., Watkins, D., Webster, M., and Wendisch, M.: Overview of the MOSAiC expedition – Snow and sea ice, *Elem. Sci. Anthropocene*, 10, 000046, https://doi.org/10.1525/elementa.2021.000046, 2022.

Notz, D., Jahn, A., Holland, M., Hunke, E., Massonnet, F., Stroeve, J., Tremblay, B., and Vancoppenolle, M.: The CMIP6 Sea-Ice Model Intercomparison Project (SIMIP): understanding sea ice through climate-model simulations, *Geosci. Model Dev.*, 9, 3427-3446, https://doi.org/10.5194/gmd-9-3427-2016, 2016.

Ortega, P., Blockley, E. W., Køltzow, M., Massonnet, F., Sandu, I., Svensson, G., Acosta Navarro, J. C., Arduini, G., Batté, L., Bazile, E., Chevallier, M., Cruz-García, R., Day, J. J., Fichefet, T., Flocco, D., Gupta, M., Hartung, K., Hawkins, E., Hinrichs, C., Magnusson, L., Moreno-Chamarro, E., Pérez-Montero, S., Ponsoni, L., Semmler, T., Smith, D., Sterlin, J., Tjernström, M., Välisuo, I., and Jung, T.: Improving Arctic Weather and Seasonal Climate Prediction: Recommendations for Future Forecast Systems Evolution from the European Project APPLICATE. *Bull. Amer. Meteor. Soc.*, 103, E2203–E2213, https://doi.org/10.1175/BAMS-D-22-0083.1, 2022.

Polyakov, I. V., Pnyushkov, A. V., Alkire, M. B., Ashik, I. M., Baumann, T. M., Carmack, E. C., Goszczko, I., Guthrie, J., Ivanov, V. V., Kanzow, T., Krishfield, R., Kwok, R., Sundfjord, A., Morison, J., Rember, R., and Yulin, A.: Greater role for Atlantic inflows on sea-ice loss in the Eurasian Basin of the Arctic Ocean. *Science*, 356, 285–291, https://doi.org/10.1126/science.aai8204, 2017.

1138 Polyakov, I. V, Ingvaldsen, R. B., Pnyushkov, A. V., Bhatt, U. S., Francis, J. A., Janout, M.,
1139 Kwok, R., and Skagseth, Ø: Fluctuating Atlantic inflows modulate Arctic atlantification.
1140 *Science*, 381, 972-979, https://doi.org/10.1126/science.adh5158, 2023.
1141 Rabe, B., Heuzé, C., Regnery, J., Aksenov, Y., Allerholt, J., Athanase, M., Bai, Y., Basque, C.,
1142 Bauch, D., Baumann, T. M., Chen, D., Cole, S. T., Craw, L., Davies, A., Damm, E.,
1143 Dethloff, K., Divine, D. V., Doglioni, F., Ebert, F., Fang, Y.-C., Fer, I., Fong, A. A.,
1144 Gradinger, R., Granskog, M. A., Graupner, R., Haas, C., He, H., He, Y., Hoppmann, M.,
1145 Janout, M., Kadko, D., Kanzow, T., Karam, S., Kawaguchi, Y., Koenig, Z., Kong, B.,
1146 Krishfield, R. A., Krumpen, T., Kuhlmey, D., Kuznetsov, I., Lan, M., Laukert, G., Lei, R.,
1147 Li, T., Torres-Valdés, S., Lin, L., Lin, L., Liu, H., Liu, N., Loose, B., Ma, X., McKay, R.,
1148 Mallet, M., Mallett, R. D. C., Maslowski, W., Mertens, C., Mohrholz, V., Muilwijk, M.,
1149 Nicolaus, M., O'Brien, J. K., Perovich, D., Ren, J., Rex, M., Ribeiro, N., Annette, A.,
1150 Schaffer, J., Schuffenhauer, I., Schulz, K., Shupe, M. D., Shaw, W., Sokolov, V.,
1151 Sommerfeld, A., Spreen, G., Stanton, T., Stephens, M., Su, J., Sukhikh, N., Sundfjord, A.,
1152 Thomisch, K., Tippenhauer, S., Toole, J. M., Vredenborg, M., Walter, M., Wang, H., Wang,
1153 L., Wang, Y., Wendisch, M., Zhao, J., Zhou, M., and Zhu, J.: Overview of the MOSAiC
1154 expedition: Physical oceanography, *Elem. Sci. Anthropocene*, 10, 00062,
1155 https://doi.org/10.1525/elementa.2021.00062, 2022.
1156 Rahmstorf, S.: Climate drift in an ocean model coupled to a simple, perfectly matched
1157 atmosphere. *Clim. Dyn.*, 11, 447–458, https://doi.org/10.1007/BF00207194, 1995.
1158 Rantanen, M., Karpechko, A. Y., Lipponen, A., Nordling, K., Hyvärinen, O., Ruosteenoja, K.,
1159 Vihma, T., and Laaksonen, A.: The Arctic has warmed nearly four times faster than the
1160 globe since 1979. *Commun. Earth Environ.*, 3, 168, https://doi.org/10.1038/s43247-022-
1161 00498-3, 2022.
1162 Ricker, R., Hendricks, S., Kaleschke, L., Tian-Kunze, X., King, J., and Haas, C.: A weekly
1163 Arctic sea-ice thickness data record from merged CryoSat-2 and SMOS satellite data, *The*
1164 *Cryosphere*, 11, 1607–1623, https://doi.org/10.5194/tc-11-1607-2017, 2017.

Rinke, A, Cassano, J. J., Cassano, E. N., Jaiser, R., and Handorf, D.: Meteorological conditions during the MOSAiC expedition: Normal or anomalous?. *Elem. Sci. Anthropocene*, 9:1, https://doi.org/10.1525/elementa.2021.00023, 2021.

Roach, L. A., and Meier, W. N.: Sea ice in 2024. *Nat. Rev. Earth Environ.*, 6, 252–254, https://doi.org/10.1038/s43017-025-00662-1, 2025.

Screen, J., and Simmonds, I.: The central role of diminishing sea ice in recent Arctic temperature amplification. *Nature*, 464, 1334–1337, https://doi.org/10.1038/nature09051, 2010.

Sedlar, J., Tjernström, M., Rinke, A., Orr, A., Cassano, J., Fettweis, X., Heinemann, G., Seefeldt, M., Solomon, A., Matthes, H., Phillips, T., and Webster, S.: Confronting Arctic troposphere, clouds, and surface energy budget representations in regional climate models with observations. *J. Geophys. Res.-Atmos.*, 125. https://doi.org/10.1029/2019JD031783, 2020.

Serreze, M. C., Kahl, J. D., and Schnell, R. C.: Low-Level Temperature Inversions of the Eurasian Arctic and Comparisons with Soviet Drifting Station Data. *J. Climate*, 5, 615–629/630. https://doi.org/10.1175/1520-0442(1992)005<0615:LLTIOT>2.0.CO;2, 1992.

Shapiro, R.: Smoothing, filtering, and boundary effects, *Rev. Geophys.*, 8(2), 359–387, https://doi.org/10.1029/RG008i002p00359, 1970.

Shchepetkin, A. F., and McWilliams, J. C.: The Regional Ocean Modeling System: A split-explicit, free-surface, topography following coordinates ocean model, *Ocean Model.*, 9, 347-404, https://doi.org/10.1016/j.ocemod.2004.08.002, 2005.

Shupe, M. D. and Intrieri, J. M.: Cloud Radiative Forcing of the Arctic Surface: The Influence of Cloud Properties, Surface Albedo, and Solar Zenith Angle, *J. Climate*, 17, 616–628, https://doi.org/10.1175/1520-0442(2004)017<0616:CRFOTA>2.0.CO;2, 2004.

Shupe, M. D.: ShupeTurner cloud microphysics product, ARM Mobile Facility (MOS) MOSAiC (Drifting Obs – Study of Arctic Climate), *ARM Data Center [data set]*, https://doi.org/10.5439/1871015, 2022.

Shupe, M. D., Rex, M., Blomquist, B., Persson, P. O. G., Schmale, J., Uttal, T., Althausen, D., Angot, H., Archer, S., Bariteau, L., Beck, I., Bilberry, J., Bucci, S., Buck, C., Boyer, M., Brasseur, Z., Brooks, I. M., Calmer, R., Cassano, J., Castro, V., Chu, D., Costa, D., Cox, C. J., Creamean, J., Crewell, S., Dahlke, S., Damm, E., de Boer, G., Deckelmann, H., Dethloff, K., Dütsch, M., Ebell, K., Ehrlich, A., Ellis, J., Engelmann, R., Fong, A. A., Frey, M. M., Gallagher, M. R., Ganzeveld, L., Gradinger, R., Graeser, J., Greenamyer, V., Griesche, H., Griffiths, S., Hamilton, J., Heinemann, G., Helmig, D., Herber, A., Heuzé, C., Hofer, J., Houchens, T., Howard, D., Inoue, J., Jacobi, H.-W., Jaiser, R., Jokinen, T., Jourdan, O., Jozef, G., King, W., Kirchgaessner, A., Klingebiel, M., Krassovski, M., Krumpen, T., Lampert, A., Landing, W., Laurila, T., Lawrence, D., Lonardi, M., Loose, B., Lüpkes, C., Maahn, M., Macke, A., Maslowski, W., Marsay, C., Maturilli, M., Mech, M., Morris, S., Moser, M., Nicolaus, M., Ortega, P., Osborn, J., Pätzold, F., Perovich, D. K., Petäjä, T., Pilz, C., Pirazzini, R., Posman, K., Powers, H., Pratt, K. A., Preußer, A., Quéléver, L., Radenz, M., Rabe, B., Rinke, A., Sachs, T., Schulz, A., Siebert, H., Silva, T., Solomon, A., Sommerfeld, A., Spreen, G., Stephens, M., Stohl, A., Svensson, G., Uin, J., Viegas, J., Voigt, C., von der Gathen, P., Wehner, B., Welker, J. M., Wendisch, M., Werner, M., Xie, Z. Q., and Yue, F.: Overview of the MOSAiC expedition: Atmosphere, *Elem. Sci. Anthropocene*, 10, 00060, https://doi.org/10.1525/elementa.2021.00060, 2022.

Tan, I., Sotiropoulou, G., Taylor, P. C., Zamora, L. and Wendisch, M.: A Review of the Factors Influencing Arctic Mixed-Phase Clouds: Progress and Outlook. In: *Clouds and Their Climatic Impacts*, Sullivan, S. C. and Hoose, C., Eds., https://doi.org/10.1002/9781119700357.ch5, 2023.

Timmermans, M.-L., and Toole, J. M.: the Arctic Ocean's Beaufort Gyre. *Ann. Rev. Mar. Sci.*, 15, 223–248, https://doi.org/10.1146/annurev-marine-032122-012034, 2023.

Turner, A. K., and Hunke, E. C.: Impacts of a mushy-layer thermodynamic approach in global sea-ice simulations using the CICE sea-ice model, *J. Geophys. Res.-Oceans*, 120, 1253–1275, https://doi.org/10.1002/2014JC010358, 2015.

Uttal, T., Curry, J. A., McPhee, M. G., Perovich, D. K., Moritz, R. E., Maslanik, J. A., Guest, P. S., Stern, H. L., Moore, J. A., Turenne, R., Heiberg, A., Serreze, M. C., Wylie, D. P., Persson, O. G., Paulson, C. A., Halle, C., Morison, J. H., Wheeler, P. A., Makshtas, A.,Welch, H., Shupe, M. D., Intrieri, J. M., Stamnes, K., Lindsay, R. W., Pinkel, R., Pegau, W. S., Stanton, T. P., Grenfeld, T. C.: The surface heat budget of the Arctic. *Bull. Am. Meteorol. Soc.*, 83, 255–275, https://doi.org/10.1175/1520-0477(2002)083<0255:SHBOTA>2.3.CO;2, 2002.

Vihma, T.: Effects of Arctic Sea Ice Decline on Weather and Climate: A Review. *Surv. Geophys.*, 35, 1175–1214, https://doi.org/10.1007/s10712-014-9284-0, 2014.

Wang Q., Shu. Q., and Wang F.: Recent emergence of Arctic atlantification dominated by climate warming. *Sci. Adv.*, 10, eadq5235 https://doi.org/10.1126/sciadv.adq5235, 2024.

Wang, Q., Shu, Q., Wang, S., Li, X., Danilov, S., Qiao, F., Song, Z., Wang, F., and Jung, T.: Dominant inflation of the Arctic Ocean's Beaufort Gyre in a warming climate. *Commun. Earth Environ.*, 6, 40, https://doi.org/10.1038/s43247-025-02028-3, 2025.

Warren, S. G.: Optical properties of ice and snow. *Phil. Trans. R. Soc. A.*, 37720180161, http://doi.org/10.1098/rsta.2018.0161, 2019.

Yang, C.-Y.: The evaluation data utilized in the manuscript: "Conservation of Heat in the Coupled Arctic Prediction System (CAPS v1.1): Comprehensive model evaluation based on the MOSAiC observations". *Zenodo [data set]*. https://doi.org/10.5281/zenodo.18764432, 2026a.

Yang, C.-Y.: The model code of Coupled Arctic Prediction System version 1.1 (CAPS v1.1) for the permanent archive in the manuscript: "Conservation of Heat in the Coupled Arctic Prediction System (v1.1): Comprehensive model evaluation based on the MOSAiC observations", *Zenodo [code]*, https://doi.org/10.5281/zenodo.18308943, 2026b.

Yang, C.-Y.: The simulated outputs analyzed in the manuscript: "Conservation of Heat in the Coupled Arctic Prediction System (v1.1): Comprehensive model evaluation based on the

MOSAiC observations", *Zenodo [data set]*, https://doi.org/10.5281/zenodo.18308549, 2026c.

Yang, C.-Y., Liu, J., and Xu, S.: Seasonal Arctic sea ice prediction using a newly developed fully coupled regional model with the assimilation of satellite sea ice observations, *J. Adv. Model. Earth Sy.*, 12, e2019MS001938, https://doi.org/10.1029/2019MS001938, 2020.

Yang, C.-Y., Liu, J., and Chen, D.: An improved regional coupled modeling system for Arctic sea ice simulation and prediction: a case study for 2018, *Geosci. Model Dev.*, 15, 1155–1176, https://doi.org/10.5194/gmd-15-1155-2022, 2022.

Yang, C.-Y., Liu, J., and Chen, D.: Understanding the influence of ocean waves on Arctic sea ice simulation: a modeling study with an atmosphere–ocean–wave–sea ice coupled model, *The Cryosphere*, 18, 1215–1239, https://doi.org/10.5194/tc-18-1215-2024, 2024.

Yao, C., Yan, Y., Zhou, Y., Xiong, Z., Xu, Y., and Uotila, P.: Comparative analysis of multiple ocean reanalysis datasets in the Arctic. *Clim. Dyn.*, 63, 347, https://doi.org/10.1007/s00382-025-07842-1, 2025.

Zhang, J. and Rothrock, D.: Modeling global sea ice with a thickness and enthalpy distribution model in generalized curvilinear coordinates. *Mon. Wea. Rev.*, 131, 845–861, https://doi.org/10.1175/1520-0493(2003)131<0845:MGSIWA>2.0.CO;2, 2003.

Zhang, J., Weijer, W., Steele, M., Cheng, W., Verma, T., and Venezaini, M.: Labrador Sea freshening linked to Beaufort Gyre freshwater release. *Nat. Commun.*, 12, 1229, https://doi.org/10.1038/s41467-021-21470-3, 2021.

6. Tables

Table 1 List of exchanged variables in CAPS with the revised coupling approach.

Variable	Source	Destination	Meaning
F_{swdn}	WRF	ROMS, CICE	Downward shortwave radiation at the surface
F_{lwdn}	WRF	ROMS, CICE	Downward longwave radiation at the surface
$F_{sh,ao}$	WRF	ROMS	Sensible heat flux at the atmosphere–ocean interface
$F_{lh,ao}$	WRF	ROMS	Latent heat flux at the atmosphere–ocean interface
$\vec{\tau}_{ao}$	WRF	ROMS	Wind stress at the atmosphere–ocean interface
$MSLP$	WRF	ROMS	Mean sea level pressure
z_a	WRF	CICE	Height of the lowest atmospheric level
θ_a	WRF	CICE	Potential temperature at the lowest atmospheric level
Q_a	WRF	CICE	Specific humidity at the lowest atmospheric level
$\vec{U}_a$	WRF	CICE	Wind fields at the lowest atmospheric level
P_{total}	WRF	ROMS, CICE	Total precipitation rate
E_{ao}	WRF	ROMS	Evaporation rate at the atmosphere–ocean interface
SST	ROMS	WRF, CICE	Sea surface temperature
SSS	ROMS	CICE	Sea surface salinity
W_{fr}	ROMS	CICE	Freezing/melting potential
$\vec{U}_o$	ROMS	CICE	Surface ocean currents
∇H_o	ROMS	CICE	Sea surface slope
A_{ice}	CICE	WRF	Sea ice concentration
T_{ice}	CICE	WRF	Ice surface temperature
α_{ice}	CICE	WRF	Surface albedo of snow and ice
$F_{sh,ai}$	CICE	WRF	Sensible heat flux at the atmosphere–ice interface
$F_{lh,ai}$	CICE	WRF	Latent heat flux at the atmosphere–ice interface
$F_{swthru,io}$	CICE	ROMS	Penetrated shortwave radiation through sea ice
$F_{heat,io}$	CICE	ROMS	Net heat flux at the ice–ocean interface
$F_{water,io}$	CICE	ROMS	Freshwater flux at the ice–ocean interface
$F_{salt,io}$	CICE	ROMS	Salt flux at the ice–ocean interface
$\vec{\tau}_{io}$	CICE	ROMS	Ice–ocean stress

Table 2 The summary of physic options and details of the revised CAPS.

Horizontal grid points	320 x grid points * 440 y grid points
Horizontal grid spacing	~24 km
Vertical layers	WRF: 50 with 10 hPa as the model top ROMS: 40 CICE: 7 ice layers, 1 snow layer
Time step	WRF: 60 s WRF radiation calling interval: 15 min ROMS/CICE: 180 s Coupling frequency: 180 s
WRF physics	
Cumulus	Grell-Freitas (Freitas et al. 2018)
Microphysics	Morrison 2-moment (Morrison et al. 2009)
Longwave radiation	RRTMG (Iacono et al., 2008)
Shortwave radiation	RRTMG (Iacono et al., 2008)
Boundary layer	MYNN Level 2.5 (Nakanishi and Niino, 2006)
Land surface	Unified Noah LSM (Chen and Dudhia 2001)
ROMS physics	
Tracer advection	Upwind third-order horizontal advection with the upwind flux limiter (Leonard and Mokhtari, 1990; Shchepetkin, and McWilliams, 2005) Centered fourth-order vertical advection (Shchepetkin, and McWilliams, 2005)
Tracer vertical mixing	KPP (Large et al., 1994)
CICE physics	
Ice dynamics	EVP (Hunke and Dukowicz, 1997)
Ice thermodynamics	Bitz and Lipscomb (1999)
Shortwave albedo	Delta-Eddington (Briegleb and Light, 2007)
Melt pond	Level-ice (Hunke et al., 2013)

Table 3 Computational-cost benchmark for the original and revised CAPS coupling configurations on an HPC system with two 32-core Intel Xeon Platinum 8358P processors at 2.60 GHz and 512 GB RAM per node. SYPD: simulated years per wall-clock day. CHPY: Core-hours per simulated year. MaxRSS: the maximum resident set size. AveRSS: the average resident set size. MaxVMSize: the maximum virtual memory size.

	The original coupling	The revised coupling
Configuration	Exp_FREE_OLD	Exp_FREE
Simulated period	31 days	31 days
Core allocated	320 in total 240 for WRF 80 for ROMS/CICE	320 in total 240 for WRF 80 for ROMS/CICE
Wall time	3:04:29	3:04:33
SYPD	0.6629	0.6627
CHPY	11584.8	11588.9
Wall-time overhead	N/A	0.036 %
MaxRSS	2.56 G	3.41 G
AveRSS	0.19 G	0.19 G
MaxVMSize	4.77 G	6.47 G

Table 4 Bias and RMSE of Exp_FREE against MOSAiC observations for atmospheric, oceanic, and sea-ice variables. Atmospheric profile variables are evaluated at altitudes of 1, 3, 5, 7, and 9 km, oceanic profile variables at depths of 10, 20, 50, 75, and 100 m, and single-level variables at their corresponding observations levels.

Variable	Level	Bias	RMSE
SIT (m) / snow depth (cm)	mean	-0.38 m / 1.51 cm	0.49 m / 5.30 cm
NetSW / NetLW (W/m^2)	mean	-4.67 / 5.19 W/m^2	12.7 / 8.16 W/m^2
SH / LH (W/m^2)	mean	6.29 / -1.49 W/m^2	11.67 / 4.18 W/m^2
Air temperature (°C) / RH (%)	1 km	-0.89 °C / 1.82 %	6.27 °C / 29.00 %
	3 km	0.21 °C / -5.20 %	6.00 °C / 35.46 %
	5 km	0.45 °C / -4.58 %	6.13 °C / 33.03 %
	7 km	1.06 °C / -6.42 %	6.12 °C / 28.38 %
	9 km	3.98 °C / -13.15 %	8.24 °C / 29.28 %
Ocean temperature (°C) / salinity (psu)	10 m	0.15 °C / -0.76 psu	0.39 °C / 0.98 psu
	20 m	0.29 °C / -0.58 psu	0.50 °C / 0.81 psu
	50 m	0.52 °C / -0.58 psu	0.72 °C / 0.74 psu
	75 m	0.66 °C / -0.46 psu	0.83 °C / 0.60 psu
	100 m	0.58 °C / -0.25 psu	0.87 °C / 0.40 psu

Table 5 Same as Table 4, but for Exp_NUD.

Variable	Level	Bias	RMSE
SIT (m) / snow depth (cm)	mean	-0.05 m / 0.12 cm	0.20 m / 0.14 cm
NetSW / NetLW (W/m^2)	mean	-5.54 / 4.70 W/m^2	13.16 / 7.94 W/m^2
SH / LH (W/m^2)	mean	8.99 / -1.90 W/m^2	12.31 / 3.89 W/m^2
Air temperature (°C) / RH (%)	1 km	-0.61 °C / -2.07 %	2.77 °C / 25.34 %
	3 km	-0.42 °C / -2.44 %	2.14 °C / 30.08 %
	5 km	-0.16 °C / -4.87 %	2.09 °C / 29.24 %
	7 km	0.01 °C / -6.56 %	1.82 °C / 25.70 %
	9 km	0.61 °C / -5.74 %	2.28 °C / 20.22 %
Ocean temperature (deg) / salinity (psu)	10 m	0.11 °C / -0.87 psu	0.17 °C / 1.09 psu
	20 m	0.15 °C / -0.70 psu	0.21 °C / 0.88 psu
	50 m	0.33 °C / -0.62 psu	0.41 °C / 0.77 psu
	75 m	0.49 °C / -0.53 psu	0.61 °C / 0.65 psu
	100 m	0.46 °C / -0.30 psu	0.73 °C / 0.43 psu

7. Figures

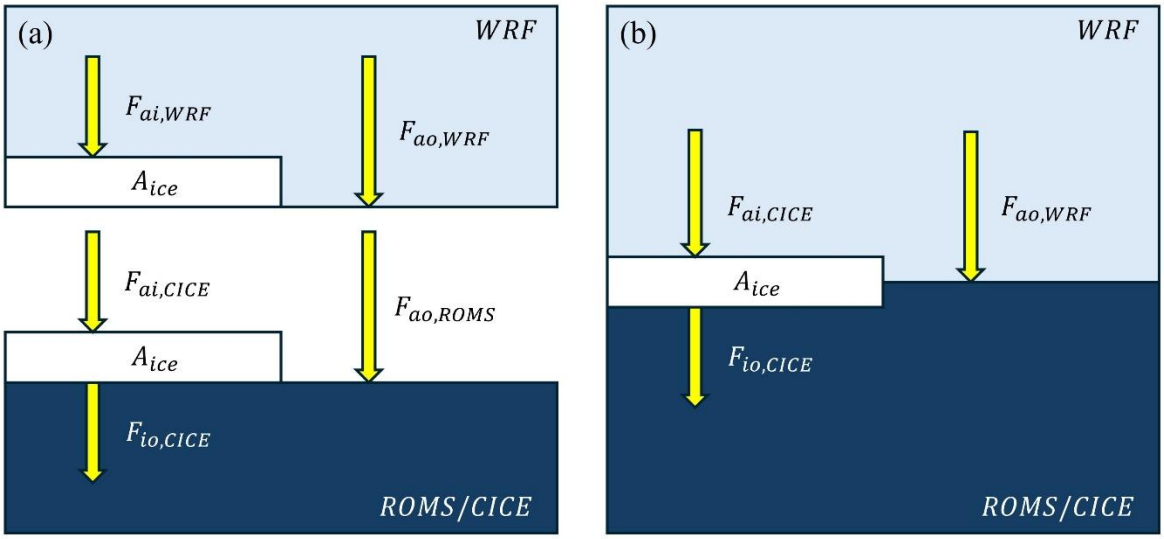


Figure 1 Pathways of surface heat fluxes exchange between WRF and ROMS/CICE in CAPS for (a) the original coupling approach, and (b) the revised coupling approach.

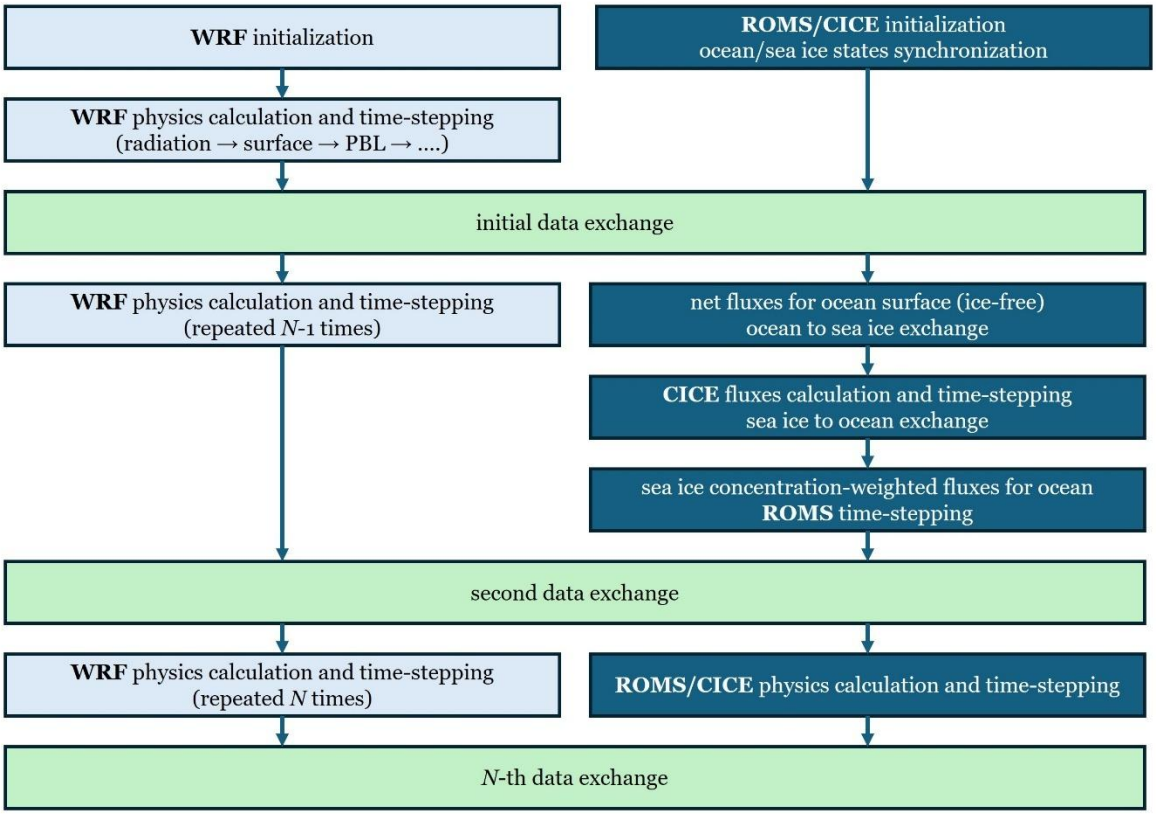


Figure 2 Schematic model sequence diagram for coupling between WRF and ROMS/CICE. The steps taken in WRF and ROMS/CICE are visualized as the light blue and dark blue blocks. The variable exchange is represented as the light green block.

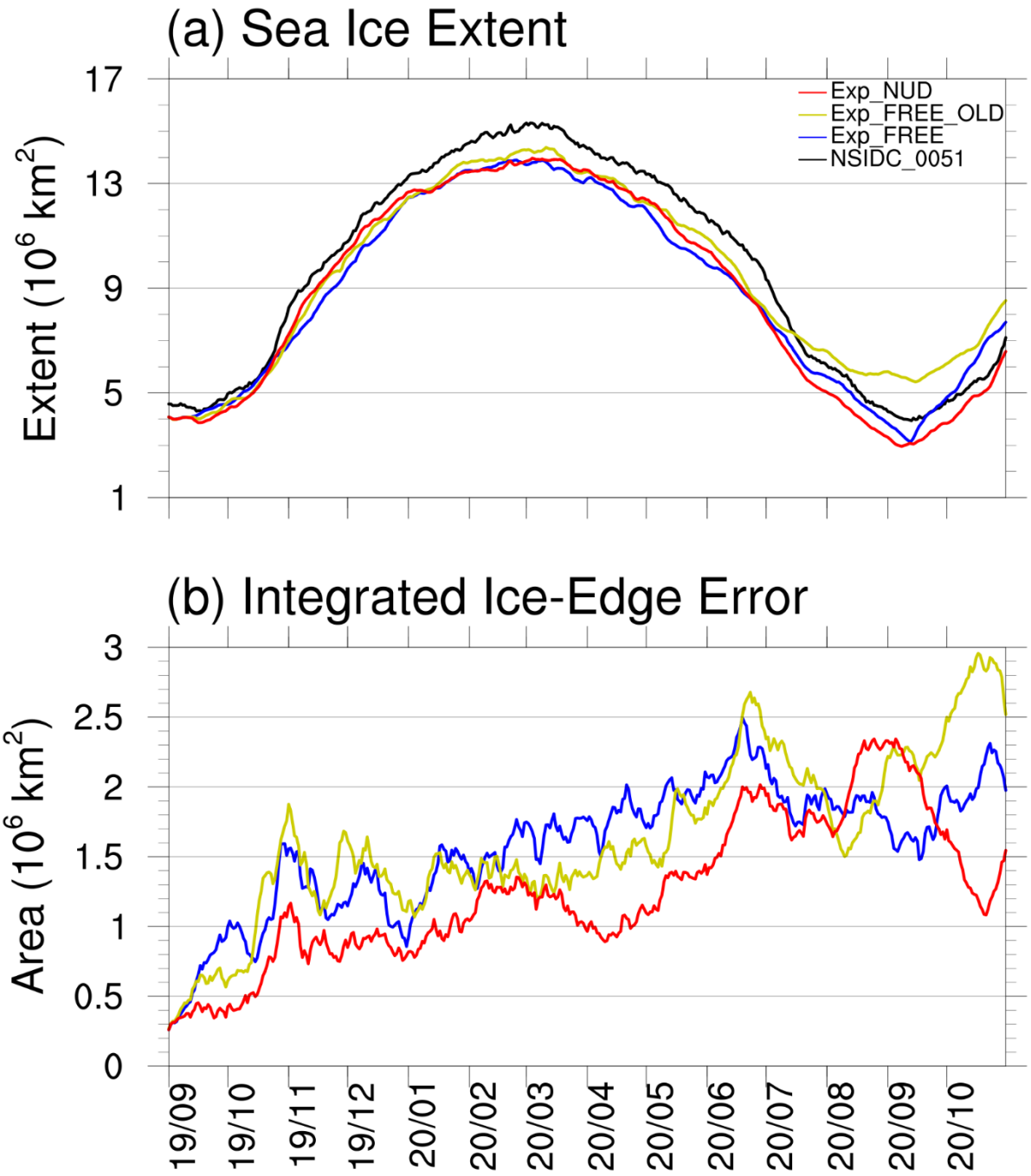


Figure 3 Time-series of (a) Arctic sea ice extent for the observations (NSIDC-0051, black line), Exp_FREE_OLD (yellow line), Exp_FREE (blue line), and Exp_NUD (red line), and (b) integrated ice-edge error for Exp_FREE_OLD, Exp_FREE, and Exp_NUD.

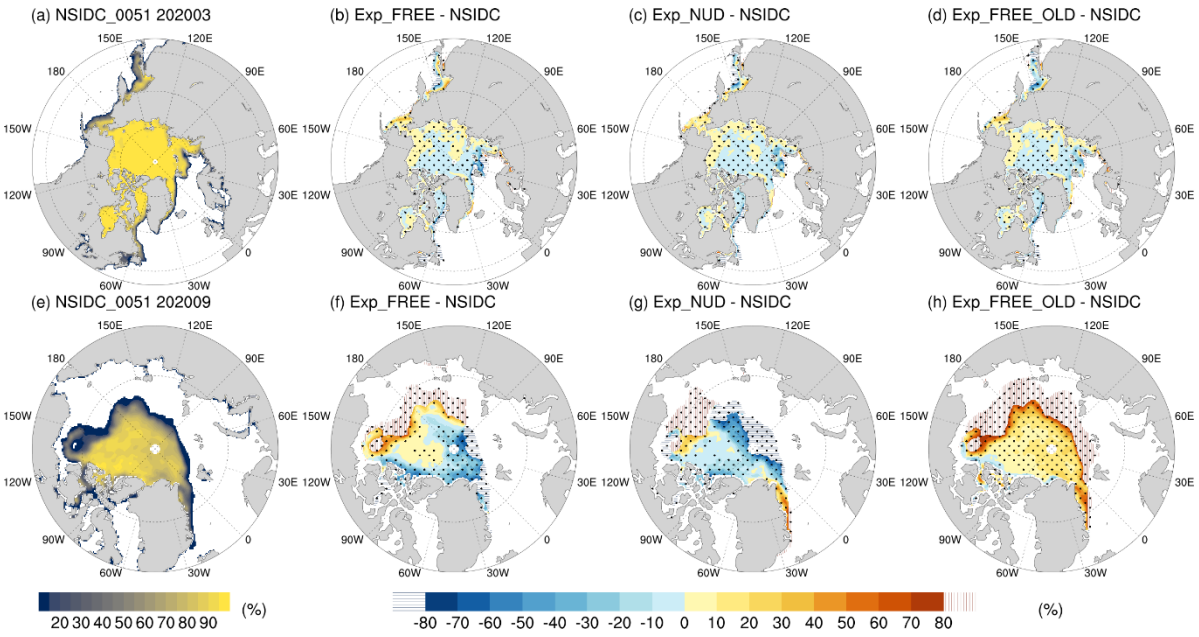


Figure 4 Monthly mean sea ice concentration (SIC) for the observations in (a) March 2020, and (e) September 2020, and the difference between the experiments and the observations for Exp_FREE, Exp_NUD, and Exp_FREE_OLD in (b–d) March 2020, and in (f–h) September 2020. Note: vertical/horizontal-lining represents the overestimated/underestimated local sea ice extent with respect to the observed local sea ice extent, following the definition of IIEE (Goessling et al., 2016); black dotted area denotes grid cells where the mean paired SIC difference is significantly different from zero based on a two-sided paired *t*-test, after Benjamini–Hochberg false discovery rate correction at $q = 0.05$.

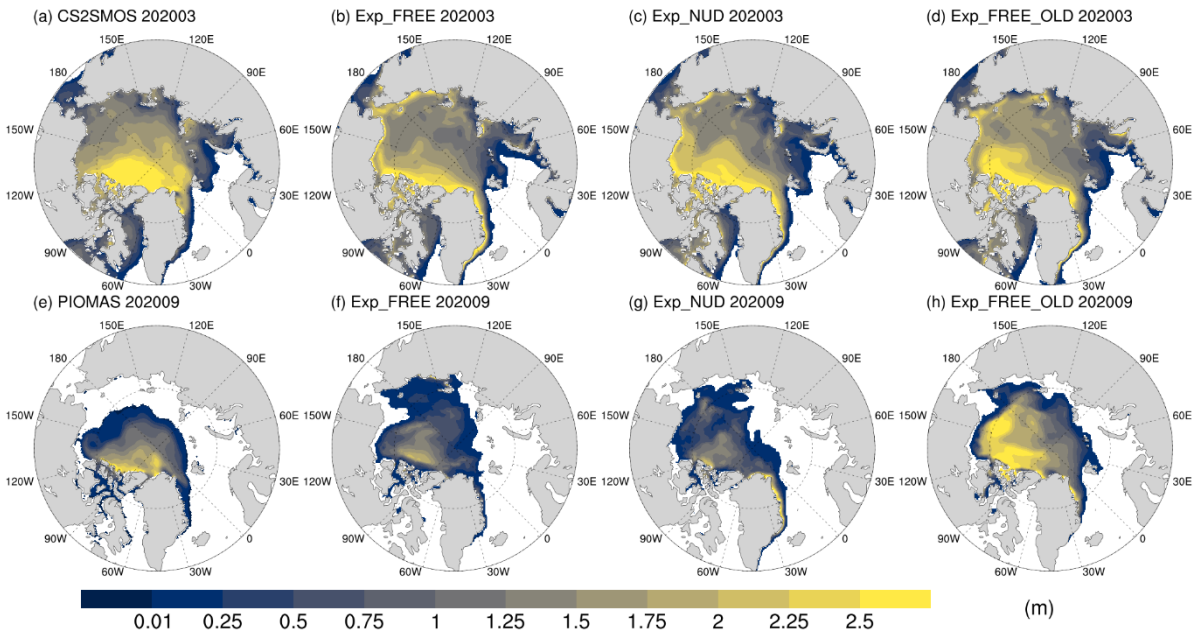


Figure 5 Monthly mean sea ice thickness for the reference data (CS2SMOS and PIOMAS), Exp_FREE, Exp_NUD, and Exp_FREE_OLD in (a-d) March 2020, and (e-h) September 2020.

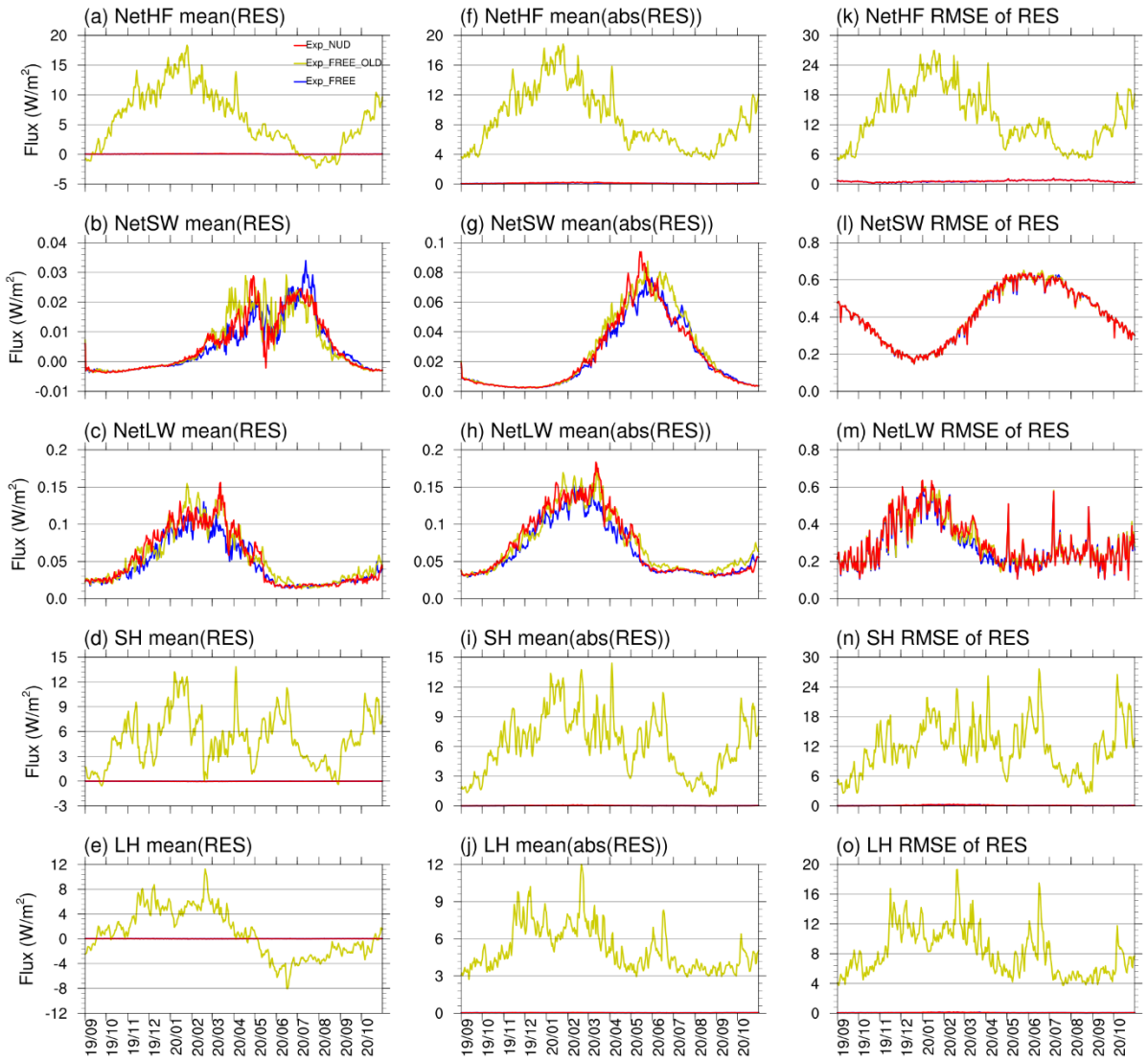


Figure 6 Domain-averaged statistics of interfacial heat-flux residuals at atmosphere–ocean–sea-ice coupling cells for all flux components in Exp_FREE_OLD (yellow line), Exp_FREE (blue line), and Exp_NUD (red line). The statistics include the (a–e) mean residual, (f–j) mean absolute residual, and (k–o) root-mean-square error (RMSE), with residuals defined by Eq. (3).

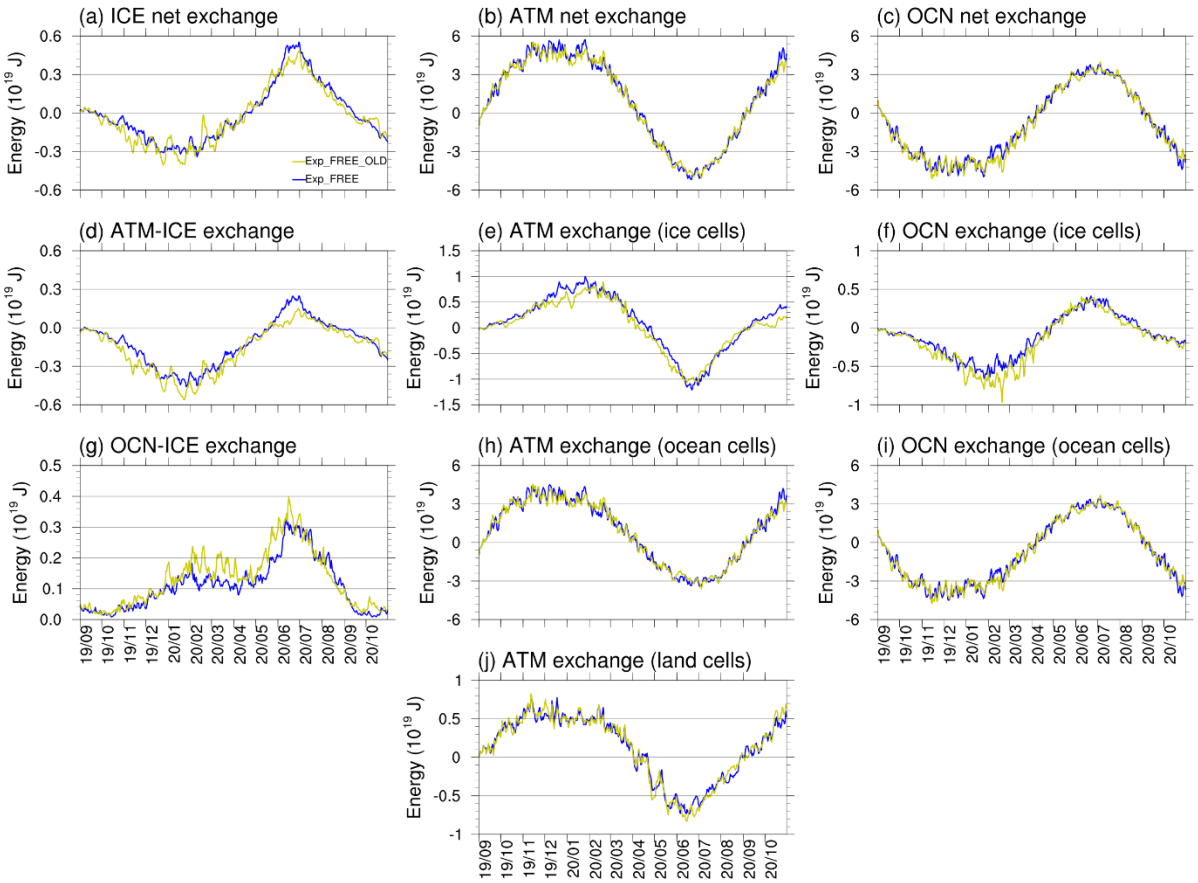


Figure 7 Daily integrated surface/interfacial energy exchange for the (a) sea-ice, (b) atmosphere, and (c) ocean in Exp_FREE_OLD (yellow line) and Exp_FREE (blue line). Sea-ice energy exchange is decomposed into (d) atmosphere–ice and (g) ice–ocean contributions; atmospheric lower-boundary exchange is separated into (e) ice-covered, (h) open-ocean, and (j) land cells; and ocean upper-boundary exchange is separated into (f) ice-covered and (i) open-ocean cells. Note: positive values indicate energy gain by the component or interface named in each panel; ice-covered cells are defined by SIC ≥ 1%.

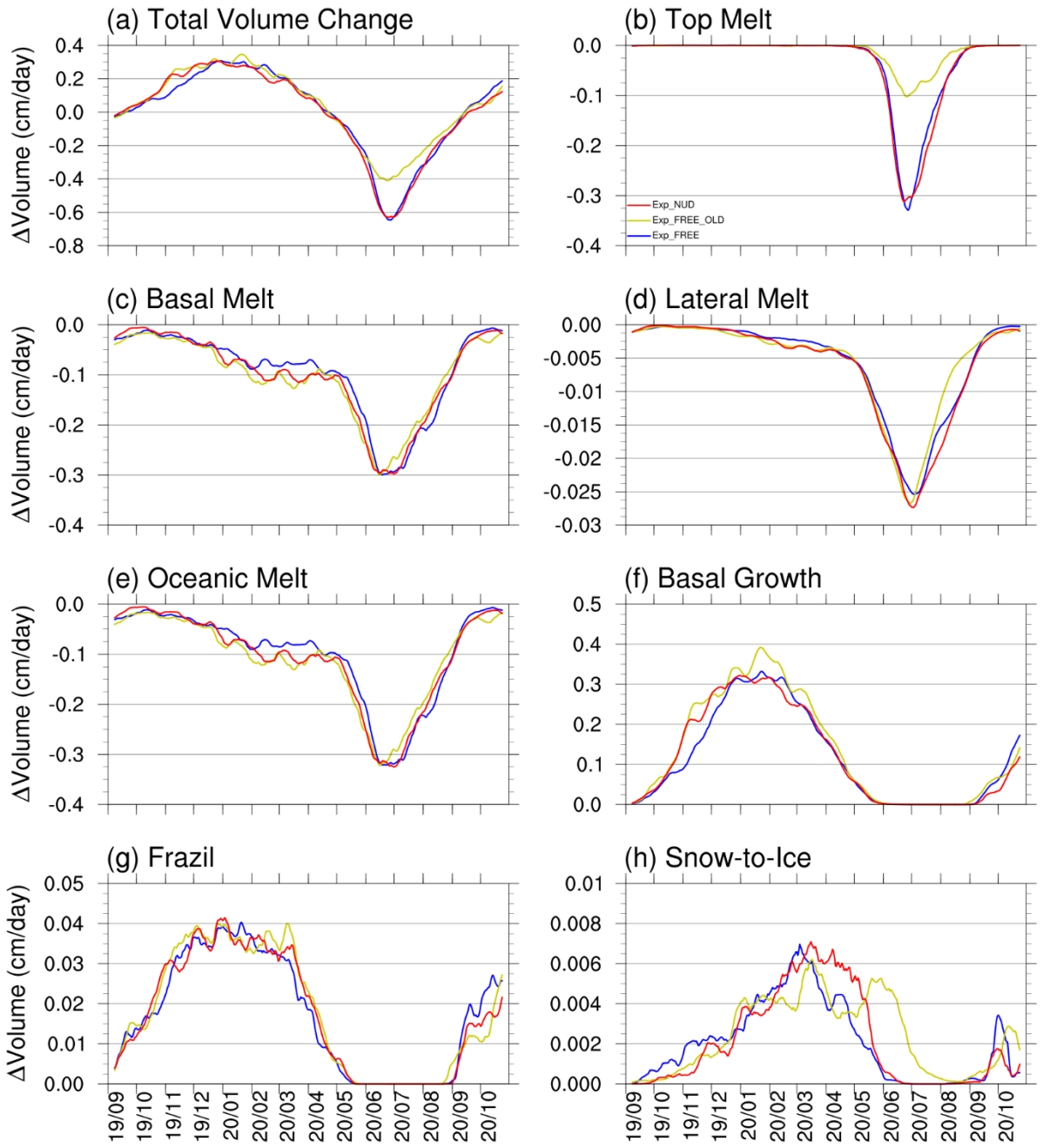


Figure 8 Time-series (15-day running-averaged) of sea ice volume budget for Exp_FREE (blue line), Exp_FREE_OLD (yellow line), and Exp_NUD (red line). Sea ice volume budgets include: (a) total volume change, (b) sea ice melt at the air-ice interface (top melt), (c) sea ice melt at the bottom of the ice (basal melt), (d) sea ice melt at the sides of the ice (lateral melt), (e) sea ice melt from oceanic energy (basal plus lateral melt), (f) sea ice growth at the bottom of the ice (basal growth), (g) sea ice growth by supercooled open water (frazil), and (h) sea ice growth due to transformation of snow to sea ice (snowice). Note: (a)-(h) are averaged over the model domain (Fig. S1).

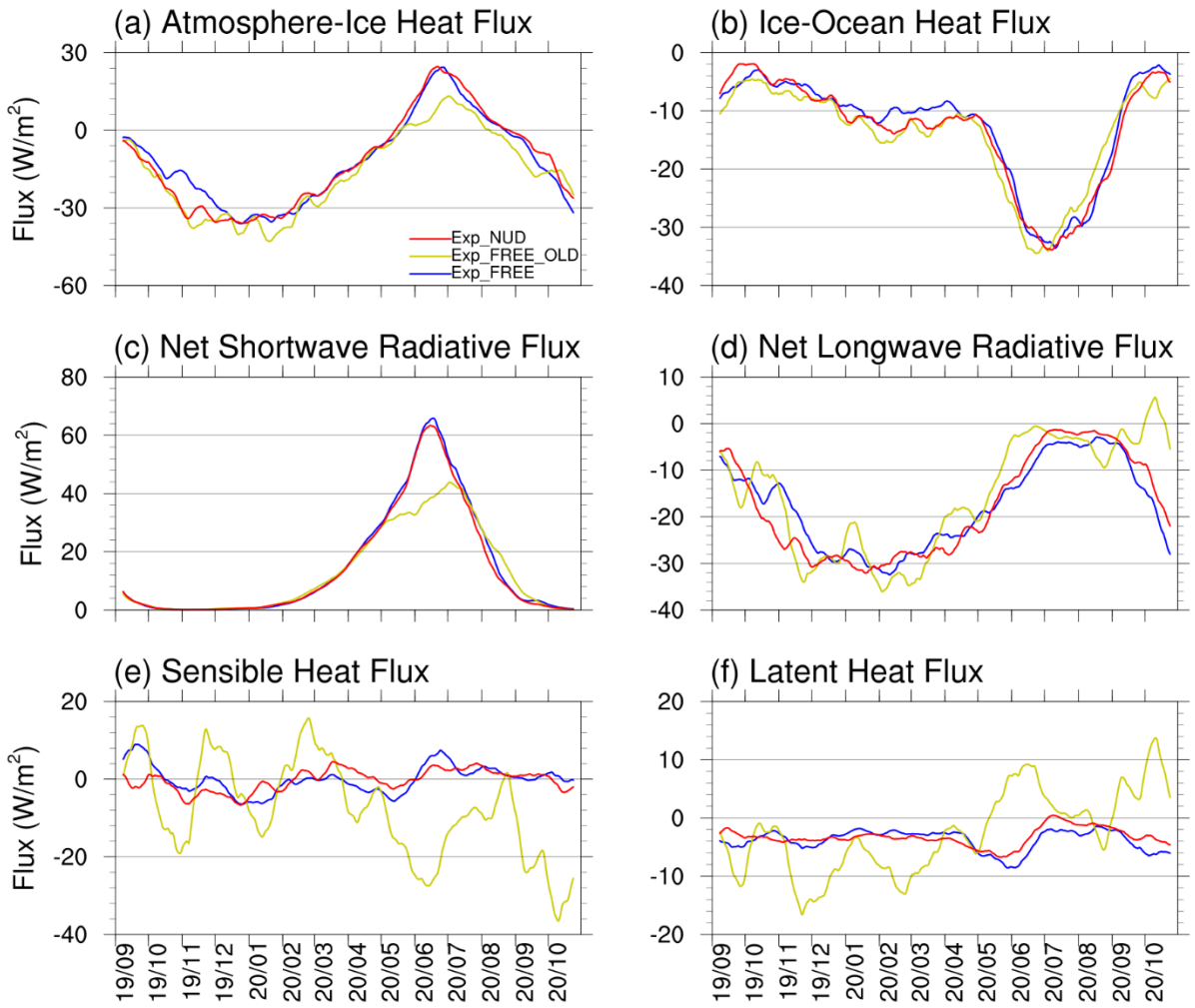


Figure 9 Time-series (15-day running-averaged) of (a) atmosphere–ice heat flux, (b) ice–ocean heat flux, (c) net shortwave radiative flux, (d) net longwave radiative flux, (e) sensible heat flux, and (f) latent heat flux for Exp_FREE (blue line), Exp_FREE_OLD (yellow line), and Exp_NUD (red line). Note: (a)-(f) are averaged with SIC-weighting over all grid cells with at least 1% SIC to represent the mean value of the grid cell, and are defined as positive downward.

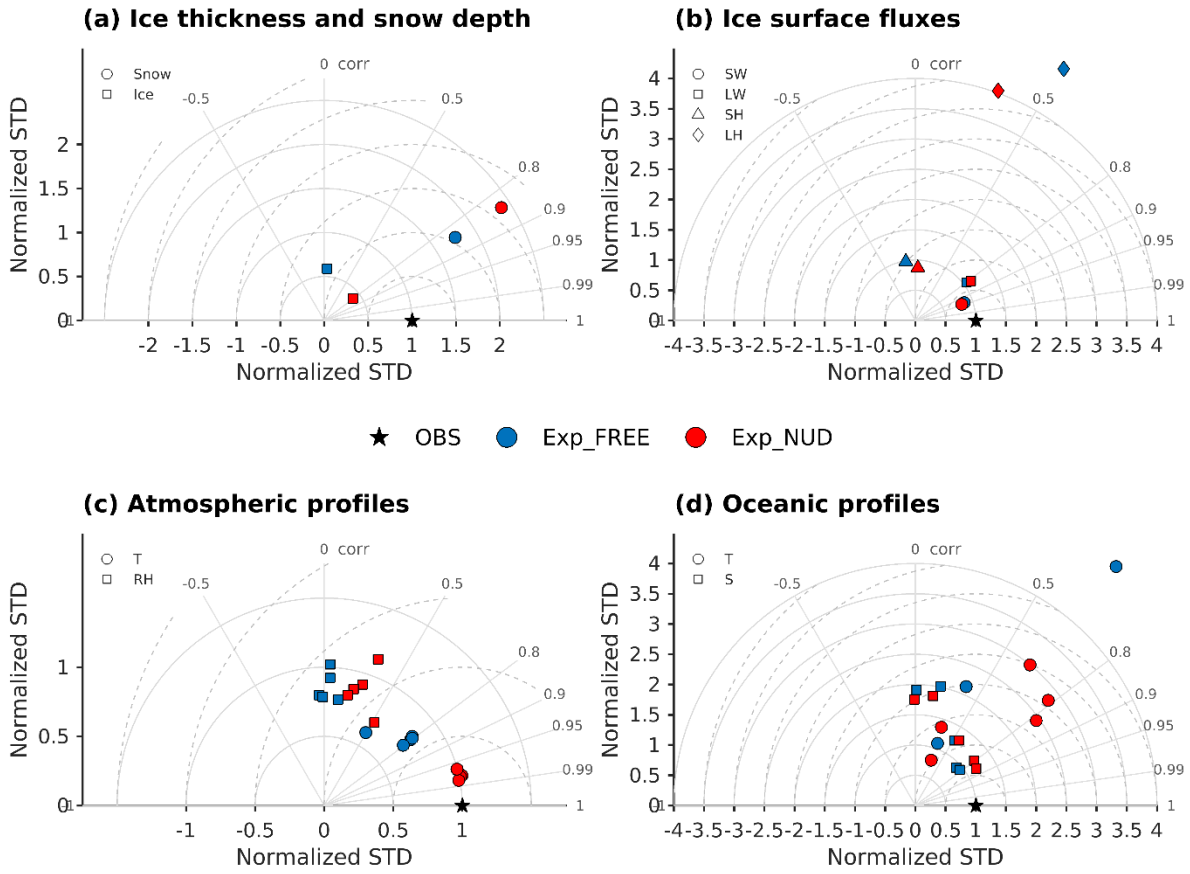


Figure 10 Taylor diagrams comparing simulated and observed (a) ice thickness and snow depth, (b) ice surface heat fluxes, (c) atmospheric profiles, and (d) ocean profiles. Atmospheric variables are evaluated at 1, 3, 5, 7, 9 km using radiosonde observations, oceanic variables at 10, 20, 50, 75, 100 m using CTD observations, and single-level sea-ice and surface variables using their corresponding observation levels. Statistics are calculated from paired model and observation samples for Exp_FREE (blue) and Exp_NUD (red). The Taylor diagrams summarize the correlation coefficient, normalized standard deviation, and normalized centered RMSE, while the corresponding bias and full RMSE are listed in Tables 4 and 5.

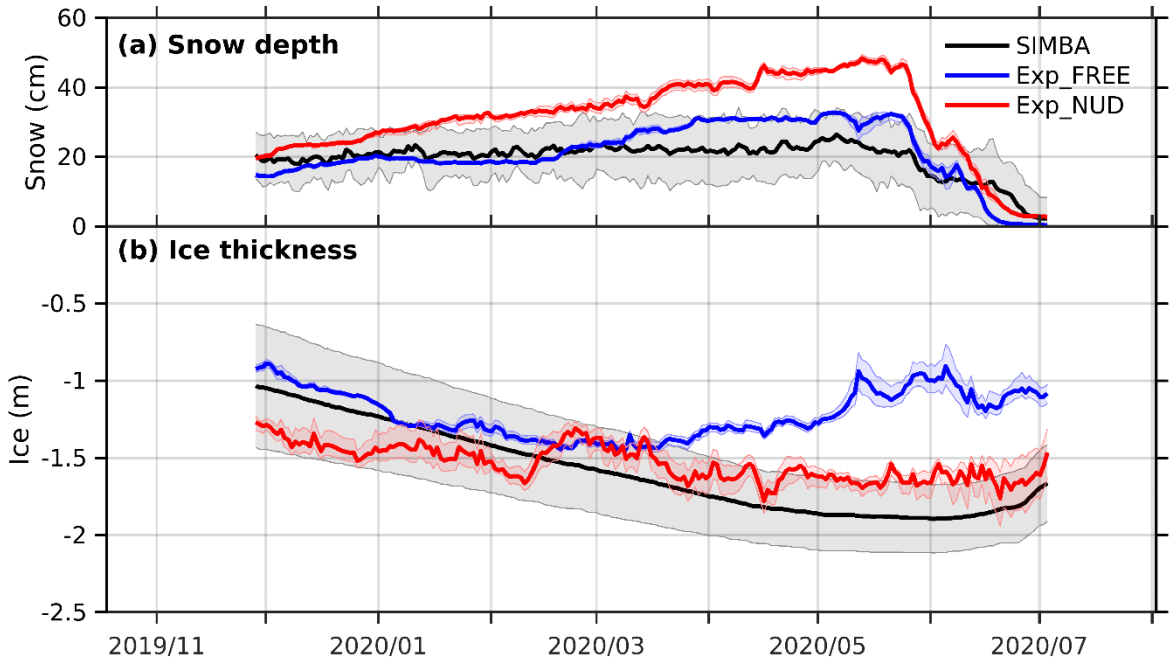


Figure 11 Time-series of daily-mean (a) snow depth and (b) sea ice thickness for SIMBA buoys (black line), Exp_FREE (blue line), and Exp_NUD (red line) along the track of MOSAiC drift. Note: the shadings represent the uncertainty range of the simulated and observed variables. For SIMBA buoys, the uncertainty range is ±1 standard deviation. For the simulations, the uncertainty range is the range of the nearest grid cell to the observed latitude/longitude and four nearby grid cells.

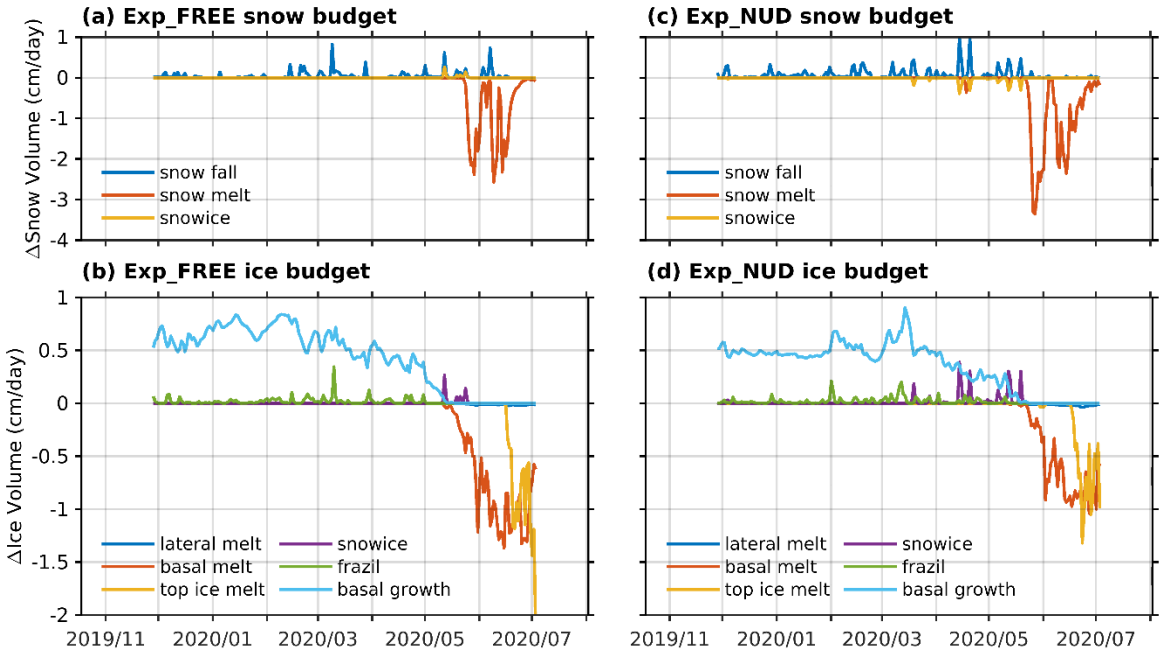


Figure 12 Time-series of snow and sea ice volume budget for (a–b) Exp_FREE, and (c–d) Exp_NUD along the track of the SIMBA buoys.

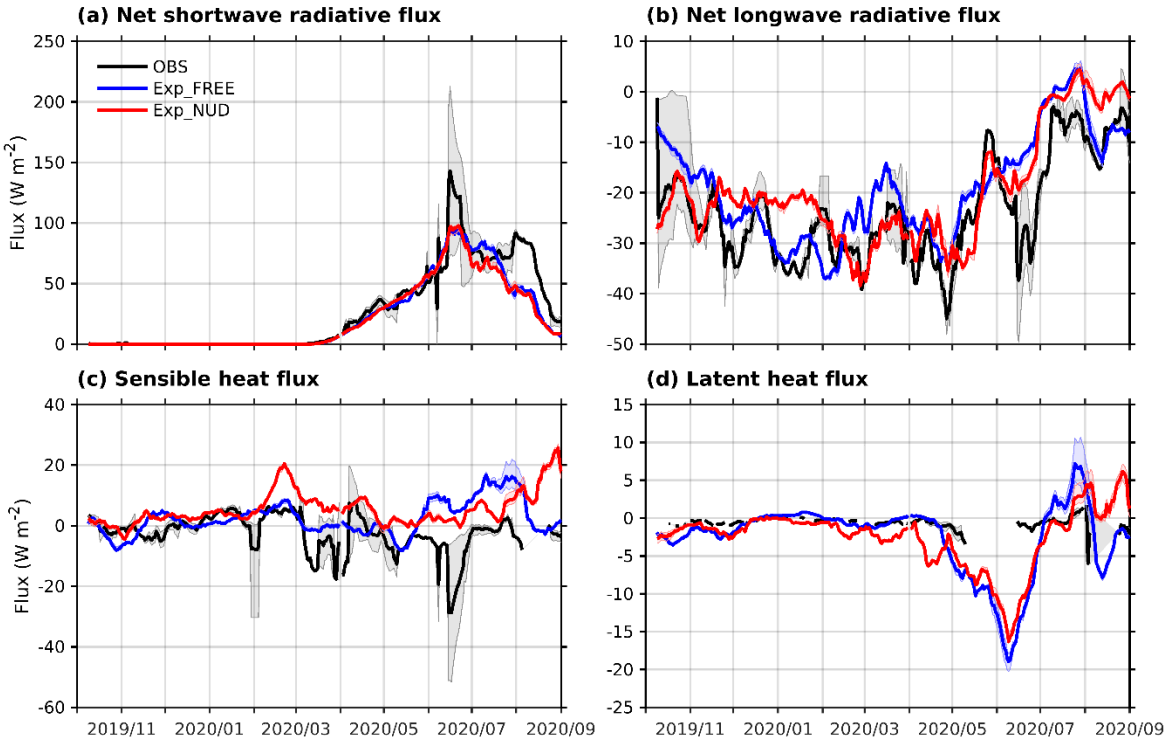


Figure 13 Time-series (15-day running-averaged) of (a) net shortwave radiative flux, (b) net longwave radiative flux, (c) sensible heat flux, and (d) latent heat flux for the observations (black line), Exp_FREE (blue line), and Exp_NUD (red line) along the track of MOSAiC drift. Note: all fluxes are defined as positive downwards. The shadings represent the uncertainty range of the simulated and observed variables. For the observations, the uncertainty range is the range of available sites with non-missing values. For the simulations, the uncertainty range is the range of the nearest grid cell to the observed latitude/longitude and four nearby grid cells.

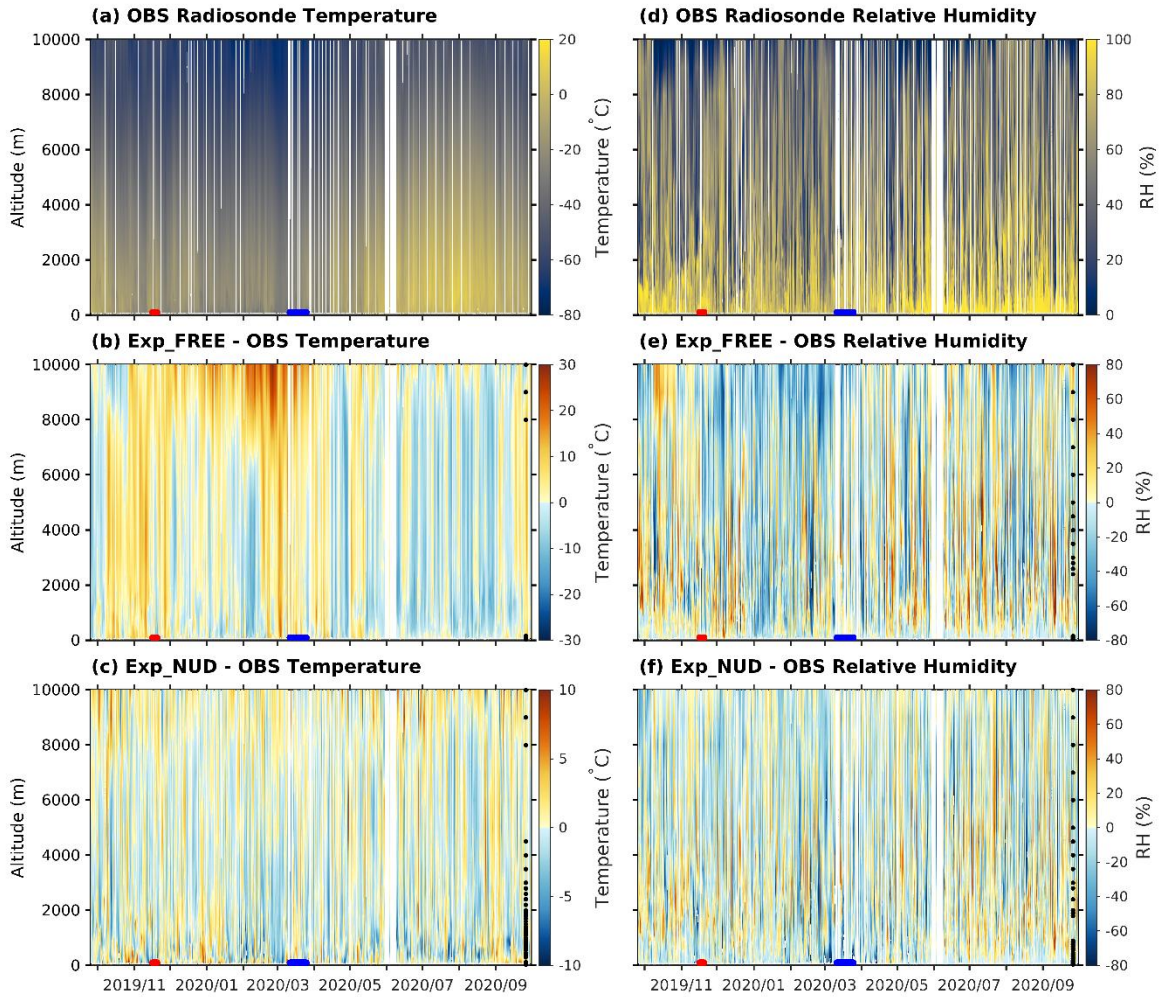


Figure 14 Time-height distributions of radiosonde observations for (a) temperature and (d) relative humidity (RH), the corresponding simulated temperature biases for (b) Exp_FREE, and (c) Exp_NUD, and the RH biases for (e) Exp_FREE, and (f) Exp_NUD along the track of MOSAiC drift. Note: red and blue lines on time-axis represent the STORM-1 and STORM-2 periods; black dots near the right edge of panels (b), (c), (e), and (f) indicate altitude levels where the full-period mean bias is significantly different from zero based on a pair moving-block bootstrap with 3-day blocks and Benjamini-Hochberg false discovery rate correction at $q = 0.05$. The horizontal position of the black dots is for visualization only and does not correspond to a specific time.

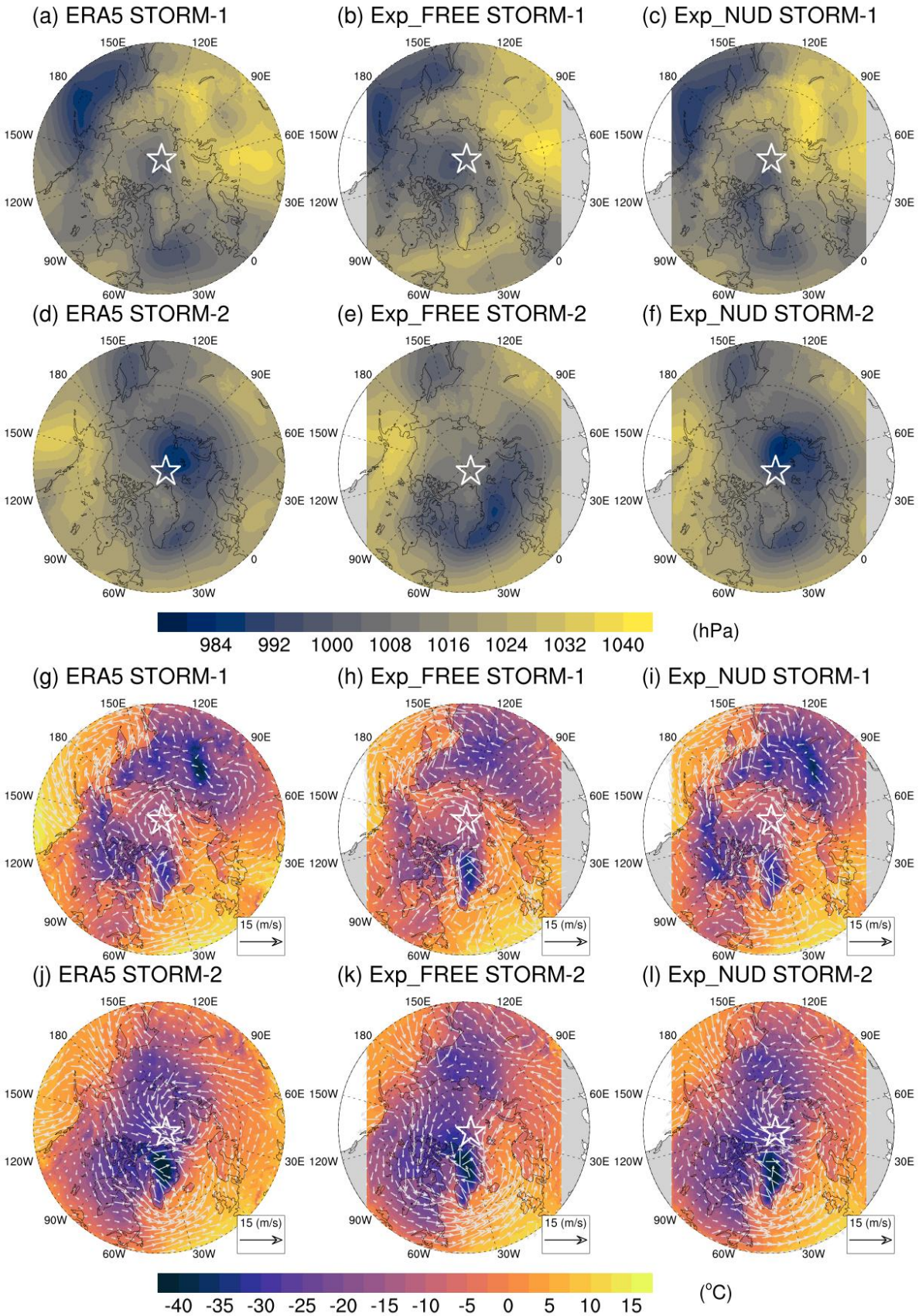

(a) ERA5 STORM-1
(b) Exp_FREE STORM-1
(c) Exp_NUD STORM-1
(d) ERA5 STORM-2
(e) Exp_FREE STORM-2
(f) Exp_NUD STORM-2
984 992 1000 1008 1016 1024 1032 1040
(hPa)
(g) ERA5 STORM-1
(h) Exp_FREE STORM-1
(i) Exp_NUD STORM-1
(j) ERA5 STORM-2
(k) Exp_FREE STORM-2
(l) Exp_NUD STORM-2
15 (m/s)
-40 -35 -30 -25 -20 -15 -10 -5 0 5 10 15
(°C)

Figure 15 The averaged mean sea level pressure of (a, d) ERA5, (b, e) Exp_FREE, and (c, f) Exp_NUD, and the averaged 2-m temperature and 10-m wind fields of (g, j) ERA5, (h, k) Exp_FREE, and (i, l) Exp_NUD during the period of STORM-1 and STORM-2. Note: white star represents the averaged location of radiosondes during the corresponding storm period, and white gap in panels of simulated fields represents out of model domain (Fig. S1).

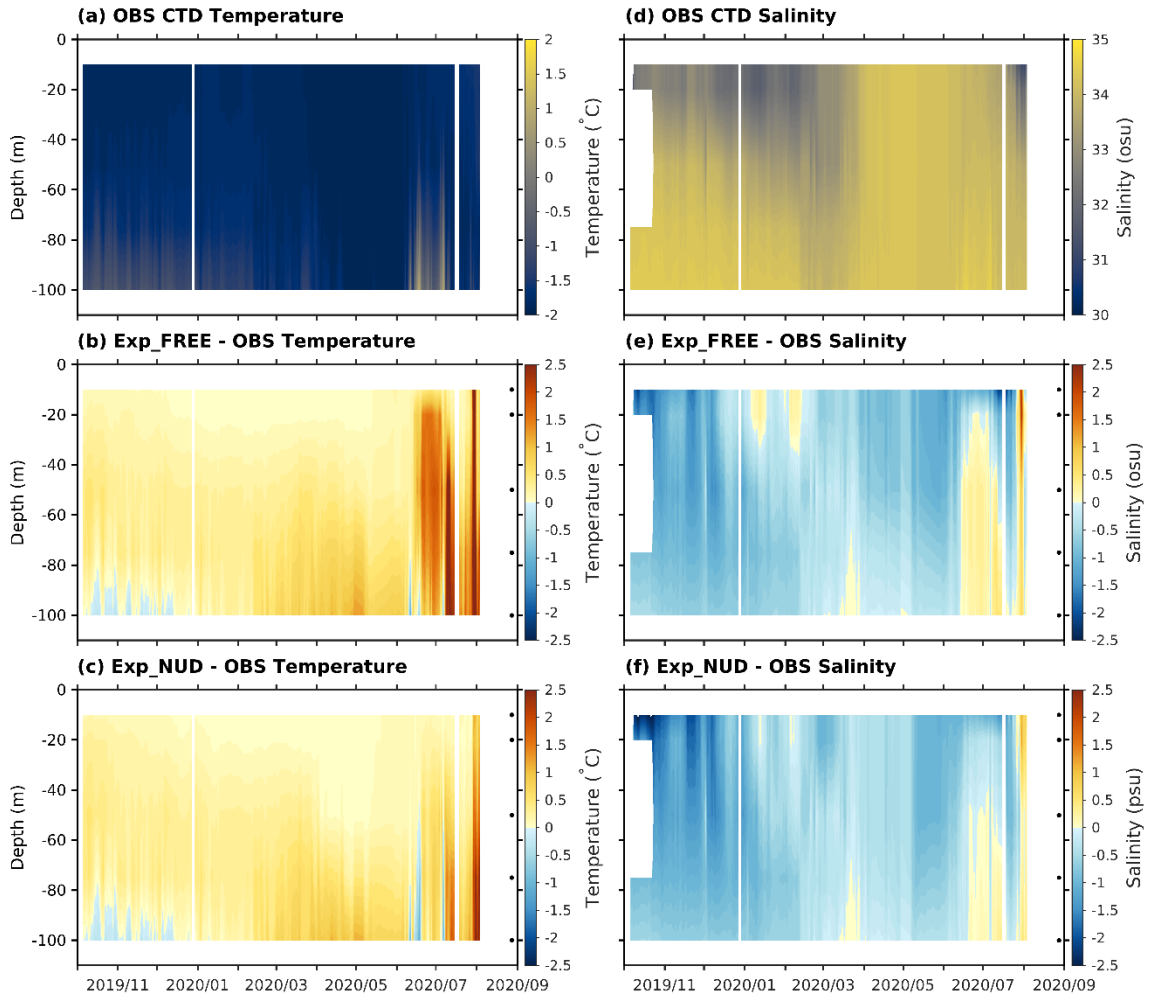


Figure 16 Time-depth distributions of CTD observations for (a) temperature and (d) salinity, the corresponding simulated temperature biases for (b) Exp_FREE, and (c) Exp_NUD, and the salinity biases for (e) Exp_FREE, and (f) Exp_NUD along the track of MOSAiC drift. Note: black dots near the right edge of panels (b), (c), (e), and (f) indicate depth levels where the full-period mean bias is significantly different from zero based on a pair moving-block bootstrap with 3-day blocks and Benjamini-Hochberg false discovery rate correction at $q = 0.05$. The horizontal position of the black dots is for visualization only and does not correspond to a specific time.

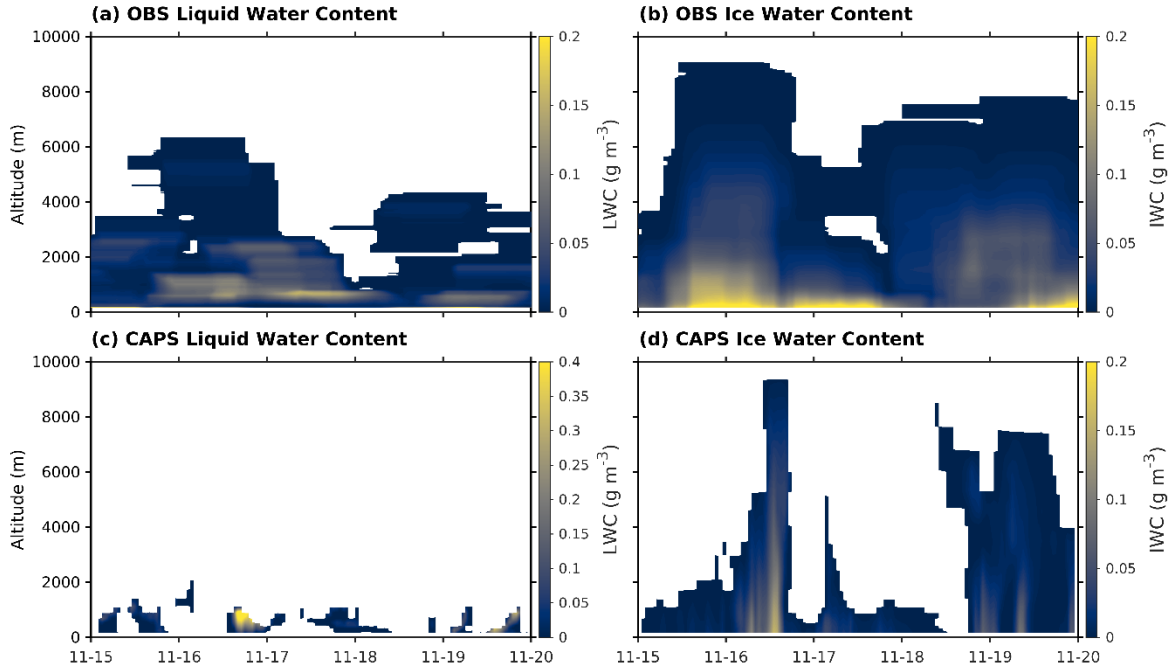


Figure 17 Time-height distributions of (a, c) liquid water content, and (b, d) ice water content for the observations and the model simulations during the STORM-1 period.